



Quantifying connectivity in the coastal ocean with application to the Southern California Bight

S. Mitarai,¹ D. A. Siegel,^{1,2} J. R. Watson,¹ C. Dong,³ and J. C. McWilliams^{3,4}

Received 22 October 2008; revised 21 April 2009; accepted 30 July 2009; published 31 October 2009.

[1] The quantification of coastal connectivity is important for a wide range of real-world applications ranging from assessment of pollutant risk to nearshore fisheries management. For these purposes, coastal connectivity can be defined as the probability that water parcels from one location have advected to another site over a given time interval. Here we demonstrate how to quantify connectivity using Lagrangian probability-density functions (PDFs) based on numerical solutions of the coastal circulation of the Southern California Bight (SCB). Ensemble mean dispersal patterns from a single release site show strong dependencies on particle-release location, season, and year, reflecting annual and interannual circulation patterns in the SCB. Mean connectivity patterns are heterogeneous for the advection time of 30 days or less, due to local circulation patterns, and they become more homogeneous for longer advection times. However, connectivity patterns for a single realization are highly variable because of intrinsic eddy-driven transport and synoptic wind-forcing variability. In the long term, mainland sites are good sources while both Northern and Southern Channel Islands are poor sources, although they receive substantial fluxes of water parcels from the mainland. The predicted connectivity gives useful information to ecological and other applications for the SCB (e.g., designing marine protected areas and predicting the impact of a pollution event) and demonstrates how high-resolution numerical solutions of coastal ocean circulations can be used to quantify nearshore connectivity.

Citation: Mitarai, S., D. A. Siegel, J. R. Watson, C. Dong, and J. C. McWilliams (2009), Quantifying connectivity in the coastal ocean with application to the Southern California Bight, *J. Geophys. Res.*, 114, C10026, doi:10.1029/2008JC005166.

1. Introduction

[2] Solutions for many important problems in the marine environment require the quantification of the connectivity of one nearshore site with another via the oceanographic advection of water parcels. For example, the assessment of risk from exposure to a pollutant from a point source requires the assessment of pollutant concentrations from the source site that have advected to all other sites in the region as a function of time [e.g., Fischer *et al.*, 1979; Grant *et al.*, 2005]. Further, many nearshore fish and invertebrates have a life cycle that includes an obligate pelagic larval stage that can last from a few days to several months [Kinlan and Gaines, 2003; Siegel *et al.*, 2003]. Due to the small size of marine larvae, advection by coastal circulations is the dominant process driving larval dispersal which will have an order one influence on their fish stock dynamics [e.g.,

Jackson and Strathmann, 1981; Roughgarden *et al.*, 1988; Cowen *et al.*, 2006].

[3] It is natural to consider the dispersal of water parcels in a Lagrangian frame and oceanographers have long tracked surface water parcels using drifting buoys to characterize Lagrangian trajectories and dispersal statistics [e.g., Poulain and Niiler, 1989; Swenson and Niiler, 1996; Dever *et al.*, 1998; LaCasce, 2008]. While surface-drifter observations have been successfully utilized to characterize regional circulation and dispersal patterns, limitations in their spatiotemporal sampling restricts their ability to address source-to-destination relationships. Even model Lagrangian analyses are generally confined to releasing a small number of numerical drifters with only qualitative description of results [e.g., Cowen *et al.*, 2006; Pfeiffer-Herbert *et al.*, 2007]. Indeed, for many important applications, connectivity is modeled using a classic advection-diffusion formalism. This approach assumes uniformity in advection and diffusivity [e.g., Roughgarden *et al.*, 1988; Gaines *et al.*, 2003; Siegel *et al.*, 2003; Largier, 2003], and hence the accuracy of these simulations of connectivity must be viewed with some reservation. Thus present knowledge of coastal connectivity under real oceanic conditions remains inadequate.

[4] Lagrangian probability-density-function (PDF) modeling approaches, introduced by Taylor [1921], have been widely used in predicting expected dispersal patterns of

¹Institute for Computational Earth System Science, University of California, Santa Barbara, California, USA.

²Department of Geography, University of California, Santa Barbara, California, USA.

³Institute of Geophysics and Planetary Physics, University of California, Los Angeles, California, USA.

⁴Department of Atmospheric and Oceanic Sciences, University of California, Los Angeles, California, USA.

materials driven by turbulent processes [e.g., *Pope, 2000; Mitarai et al., 2003*]. This approach provides an accounting of the probability that water parcels have advected from one location to another over a time interval. This accounting can be made over all possible releases, providing an estimate of the ensemble mean dispersal pattern, or for specific times or time periods, enabling the assessment of seasonal or event scale dispersal patterns. Once estimated, Lagrangian PDFs can be used to determine the expected tracer concentrations, providing an appropriate metric for quantifying coastal connectivity. The limitation in applying these approaches using field observations has been the large amount of Lagrangian trajectories required to calculate PDFs. Here we overcome this restriction using Lagrangian trajectories calculated from high resolution coastal numerical model simulations.

[5] The Southern California Bight (SCB) is one of the most intensively studied coastal regions of the world's oceans [e.g., *Sverdrup and Fleming, 1941; Hickey, 1979; Lynn and Simpson, 1987; Hickey, 1992, 1993; Harms and Winant, 1998; Bograd and Lynn, 2003; Di Lorenzo, 2003; Hickey et al., 2003; Otero and Siegel, 2004; Dong and McWilliams, 2007*]. Many studies were motivated by the 1969 Santa Barbara oil spill where more than 80,000 barrels of crude oil were released into the marine environment. This event in environmental history has led in large part to the extensive studies of the circulation of the Santa Barbara (SB) Channel and the consideration of the risks associated with pollutant releases from within the SB Channel [e.g., *Brink and Muench, 1986; Dever et al., 1998; Harms and Winant, 1998; Winant et al., 1999; Oey et al., 2004*]. While these surveys clarified synoptic circulation patterns and dispersal scales in the SB Channel, nearshore site connectivity throughout the SCB has yet to be quantified.

[6] The goal of this study is to assess nearshore site connectivity in the SCB through Lagrangian PDFs obtained from realistic circulation simulations. We simulate mean dispersal patterns from a single release-site by implementing an offline Lagrangian particle tracking method that uses the coastal circulation simulations of *Dong and McWilliams [2007]* and *Dong et al. [2009]*. We use multiple years of the simulations for 1996–2002, including the strong El Niño event in 1997–1998 and the rapid transition to strong La Niña conditions in 1998–1999. The release-position dependence, seasonal variability and interannual variability of Lagrangian PDFs are examined, and are used to deduce connectivity of the SCB for 135 nearshore sites. The obtained connectivity patterns are examined as a function of the advection time and the timescale of evaluation. The findings of this study will be valuable information for assessing the risks of pollutant exposure and for understanding marine population dynamics and regulating fish stocks.

2. Configuration of Numerical Models

2.1. ROMS

[7] We use solutions from a three-dimensional hydrodynamic model ROMS (Regional Ocean Modeling System [*Dong and McWilliams, 2007; Dong et al., 2009*]) to simulate Lagrangian trajectories for the SCB. ROMS solves the rotating primitive equations with a realistic equation of

state in a generalized sigma-coordinate system in the vertical direction and a curvilinear grid in the horizontal plane [*Shchepetkin and McWilliams, 2005*]. Three-level nested grids are employed; an outer domain covering the entire U.S. west coast at 20-km horizontal grid spacing, a second embedded domain for a larger SCB area with a 6.7-km grid resolution and the finest embedded grid has a 1-km horizontal grid resolution which is used in this study (Figure 1). The three nested grids share the same 40 s-coordinate vertical level, with a standard land-mask algorithm [*Shchepetkin and O'Brien, 1996*] and a one-way nesting approach is applied to the momentum and mass exchange from parent to daughter grids [e.g., *Penven et al., 2006*]. The lateral open-boundary conditions for outer grid comes from monthly SODA (Simple Ocean Data Assimilation [*Carton et al., 2000a, 2000b*]) global oceanic reanalysis product. The simulated flow fields are initialized as the oceanic state of December 1995 using SODA fields, and the model is integrated using a repeating forcing of a normal year (1996) until the solution reaches a quasisteady state. The model was then integrated from 1996 through 2003, forced by the 3-hourly sampled hindcast wind (see below) and SODA monthly boundary data.

[8] The momentum flux at the surface is calculated from a mesoscale reanalysis wind field. A set of nested grids with resolutions 54 km, 18 km, and 6 km were implemented with the regional atmospheric model MM5 (the 5th generation Pennsylvania State University-National Center for Atmospheric Research Mesoscale Model) by *Hughes et al. [2007]*. The coarsest resolution grid (54 km) covers eastern Pacific, and the 6 km resolution grid zooms into the SCB, so that all the nests contain the SCB region. This model configuration was forced at its lateral and surface boundaries with data from the NCEP model reanalysis [*Black, 1994*]. The lateral boundary conditions are available every 3 hours from this archive. *Conil and Hall [2006]* provide further details about model parameterizations and verification against observations. The surface heat, freshwater, and short wave radiation are from the monthly NCEP atmospheric Reanalysis 2.

[9] The simulation outputs have been validated with many available observational data for the SCB [see *Dong et al., 2009*] and will be further discussed below.

2.2. Lagrangian Particle Tracking

[10] Estimates of nearshore site connectivity are made by simulating the trajectories of many water parcels (or Lagrangian particles) released from nearshore waters. Lagrangian particles are transported passively by the three-dimensional simulated currents. Nearshore waters where Lagrangian (or fluid) particles are released are defined as all waters within 10 km from the coast, and are delineated into 135 sites (Figure 1a). The center locations of these sites are located 5 km off the coast, and distributed with an approximately 10-km spacing along the shore. Each site covers a 5-km radius area. These sites cover most of waters 100 meter deep or shallower (Figure 1b). Sites 1–62 are along the mainland. Sites 63–96 are on the shore of the Northern Channel Islands (San Miguel, Santa Ana, Santa Cruz and Anacapa Islands), and sites 97–135 are on the shore of the Southern Channel Islands (Santa Catalina, San

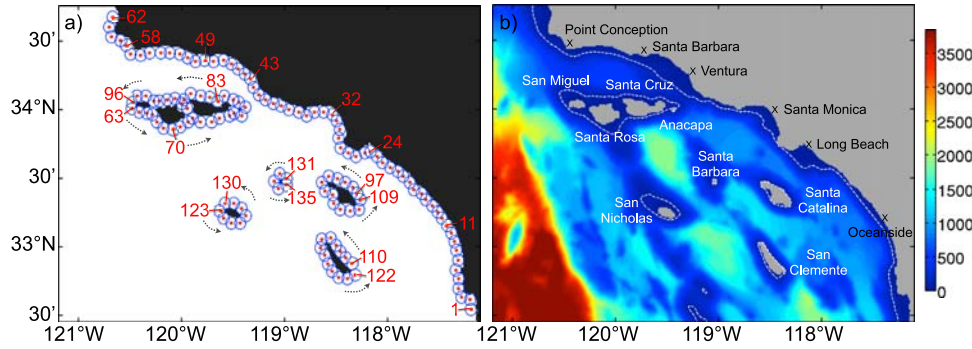


Figure 1. (a) Site locations used for the assessment of Lagrangian probability density functions and coastal connectivity. The red dots indicate the center location of each site. The blue circles indicate the area covered by each site (with a 5-km radius). The numbers indicate a given site number. The sites are categorized into three regional groups, i.e., along the mainland (sites 1–62; from south to north), Northern Channel Islands (sites 63–96), and Southern Channel Islands (sites 97–135). (b) Model bathymetry. Colors indicate water depths in meters. The white dashed line indicates the 100-m isobath. The full model domain is shown.

Clemente, San Nicholas and Santa Barbara). Sixty nine to eighty Lagrangian particles are released from each site near the top surface (5 meters below the surface) every 12 hours from 1 January 1996 through 31 December 2002, uniformly over the site. The total number of Lagrangian particles released from each site is 352,866–409,120, and sufficient to resolve spatial patterns of Lagrangian PDFs and the resulting connectivity (see below).

[11] Fluid particle properties (e.g., position, velocity, material concentrations, etc) can be expressed as functions of the initial position \mathbf{a} and advection time τ [Corrsin, 1962; Pope, 2000]. The position of the n th (realization of) fluid particle, $\mathbf{X}_n(\tau, \mathbf{a})$, evolves as

$$\frac{\partial}{\partial \tau} \mathbf{X}_n(\tau, \mathbf{a}) = \mathbf{U}_n(\tau, \mathbf{a}), \quad (1)$$

where $\mathbf{U}_n(\tau, \mathbf{a})$ indicates the velocity of the n th Lagrangian particle. The particle velocity is determined by evaluating the Eulerian flow fields at the particle's location,

$$\mathbf{U}_n(\tau, \mathbf{a}) = \mathbf{u}[\mathbf{X}_n(\tau, \mathbf{a}), t_n + \tau], \quad (2)$$

where $\mathbf{u}(\mathbf{x}, t)$ is the Eulerian velocity at a given location \mathbf{x} and time t , and t_n indicates the release time of the n th Lagrangian particle. Lagrangian particles are tracked by integrating equations (1) and (2) using a fourth-order Adams-Bashford-Moulton predictor-corrector scheme [e.g., Carr et al., 2008; Durran, 1999], given the initial location, $\mathbf{X}_n(0, \mathbf{a}) = \mathbf{a}$. The Eulerian velocity at a given particle location is estimated through linear interpolation of the discrete velocity fields. We tracked Lagrangian particles with a 15-minute time step for 120 days or until they cross the boundaries.

2.3. Estimating Lagrangian PDFs and Quantifying Coastal Connectivity

[12] A Lagrangian PDF describes the probability density function of particle displacement for a given advection

time τ . A discrete representation of Lagrangian PDFs, $f'_X(\boldsymbol{\xi}; \tau, \mathbf{a})$, can be determined as

$$f'_X(\boldsymbol{\xi}; \tau, \mathbf{a}) = \frac{1}{N} \sum_{n=1}^N \delta(\mathbf{X}_n(\tau, \mathbf{a}) - \boldsymbol{\xi}), \quad (3)$$

where N is the total number of Lagrangian particles, δ is the Dirac delta function, and $\boldsymbol{\xi}$ is the sample space variable for \mathbf{X} . We focus only on the evaluation of $f'_X(\boldsymbol{\xi}; \tau, \mathbf{a})$ in the horizontal directions. Discrete Lagrangian PDFs are evaluated from the center location of the sites defined above, averaged over each site, i.e.,

$$f'_X(\boldsymbol{\xi}; \tau, \mathbf{a}) \approx \frac{1}{\pi R^2} \int_{|\mathbf{r}| \leq R} f'_X(\boldsymbol{\xi}; \tau, \mathbf{a} + \mathbf{r}) d\mathbf{r}, \quad (4)$$

where R is the radius of each site (5 km). A Lagrangian PDF, denoted as $f_X(\boldsymbol{\xi}; \tau, \mathbf{a})$, is given by spatially filtering a discrete PDF in the sample space, i.e.,

$$f_X(\boldsymbol{\xi}; \tau, \mathbf{a}) \approx \int_{-\infty}^{\infty} G(\mathbf{x} - \boldsymbol{\xi}) f'_X(\boldsymbol{\xi}; \tau, \mathbf{a}) d\mathbf{x}, \quad (5)$$

where $G(\mathbf{x} - \boldsymbol{\xi})$ is an isotropic Gaussian filter with a standard deviation of 4 km. Values of a Lagrangian PDF represent the number of particles in km^{-2} .

[13] Lagrangian PDFs can be utilized to describe expected dispersal patterns of materials, neglecting molecular diffusion and chemical reactions, given the initial distributions of material concentrations, $c(\mathbf{x}, t_0)$. The expected concentration of the materials after a time interval τ , $\langle c(\mathbf{x}, t_0 + \tau) \rangle$, can be determined as

$$\langle c(\mathbf{x}, t_0 + \tau) \rangle = \int_{-\infty}^{\infty} c(\mathbf{a}, t_0) f_X(\mathbf{x}; \tau, \mathbf{a}) d\mathbf{a}. \quad (6)$$

This states that the expected concentration at a point is the initial concentration carried by a particle times the probability of the particle being there, integrated over all

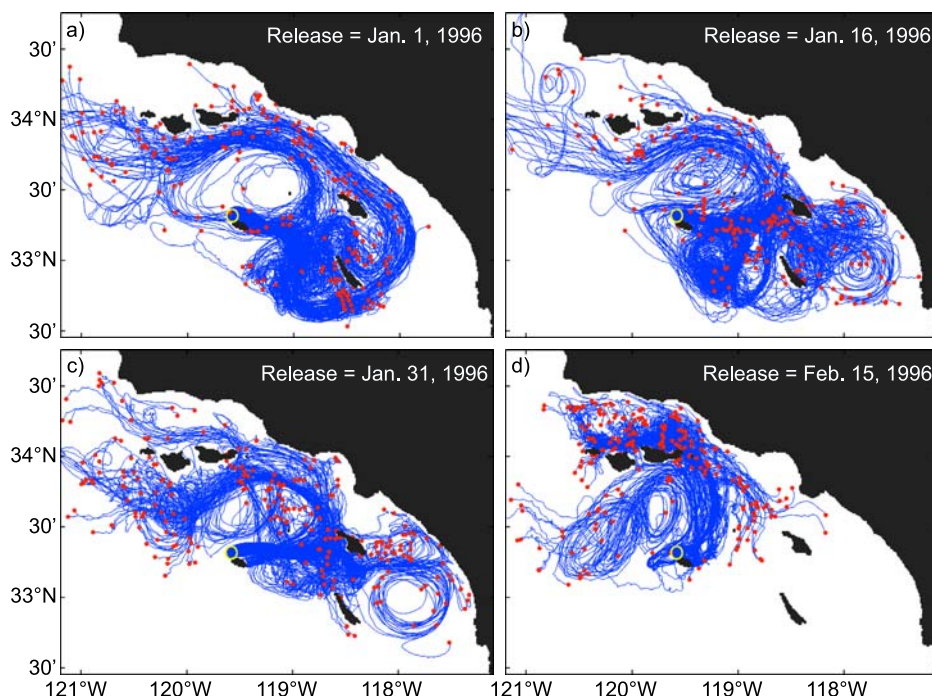


Figure 2. Sample Lagrangian particle trajectories from a single site. These Lagrangian particles are released in the nearshore of San Nicholas Island (yellow circles; site 130), on (a) 1 January 1996, (b) 16 January 1996, (c) 31 January 1996, and (d) 15 February 1996, and are transported passively by the simulated flow fields. The blue lines indicate simulated 30-day trajectories. The red dots indicate the particle locations 30 days after the release. The full model domain is shown.

particles that could be there [Tennekes and Lumley, 1972]. Different observation times can be assessed by changing the time of release enabling both the assessment of a single release at different time and over particular timescales (i.e., a given year or season or ensemble of seasons). The effects of turbulent mixing and chemical (biological) reactions of materials in altering dispersal patterns are discussed in Appendix A.

[14] Coastal connectivity is defined as the probability a water parcel leaving a source site j arrives a destination site i over a time interval τ , and is denoted here as $C_{ji}(\tau)$. Values of $C_{ji}(\tau)$ are evaluated from the Lagrangian PDF for a source location (\mathbf{x}_j) and a destination location (\mathbf{x}_i) as

$$C_{ji}(\tau) = f_X(\boldsymbol{\xi} = \mathbf{x}_i; \tau, \mathbf{a} = \mathbf{x}_j) (\pi R^2), \quad (7)$$

where the normalization by πR^2 converts probability densities to probabilities. Connectivity matrices describe the probability for the event that a water parcel is transported from site j to site i . Based upon the site locations shown in Figure 1, this results in a 135×135 matrix, $C_{ji}(\tau)$, which we define here as the connectivity matrix. Connectivity matrices are a function of the advection time τ . We evaluate Lagrangian PDFs and resulting connectivity matrices for $\tau = 1, 2, \dots, 120$ days, and use $\tau = 30$ days as a default case.

[15] Values of the destination strength, $D_i(\tau)$, measure the relative “attractiveness” of site i for all of the Lagrangian particles released in the domain for a release time of τ . $D_i(\tau)$

is calculated by summing the connectivity matrix over all source sites in the domain, i.e.,

$$D_i(\tau) = \sum_{j \in J} C_{ji}(\tau), \quad J = j_1, j_2, \dots, j_N \quad (8)$$

Similarly, the source strength, $S_j(\tau)$, which measures the relative success that a site’s particles encounter another site within a timescale τ , can be calculated as

$$S_j(\tau) = \sum_{i \in I} C_{ji}(\tau), \quad I = i_1, i_2, \dots, i_M \quad (9)$$

Distributions of source and destination strength are useful for helping illustrate features of the calculated connectivity matrices.

3. Lagrangian PDFs in the Southern California Bight

3.1. Turbulent Dispersion and Examples of Expected Dispersal Patterns

[16] Lagrangian trajectories for particles released off San Nicholas Island (site 130) illustrate the quasichaotic nature of turbulent transport in the coastal ocean (Figure 2). The simulated trajectories clearly show sensitivity to the date of release. For example, many Lagrangian particles released from this site on 31 January 1996 are transported toward the northeast and after 30 days are found relatively close to the sites between the Northern and Southern Channel Islands

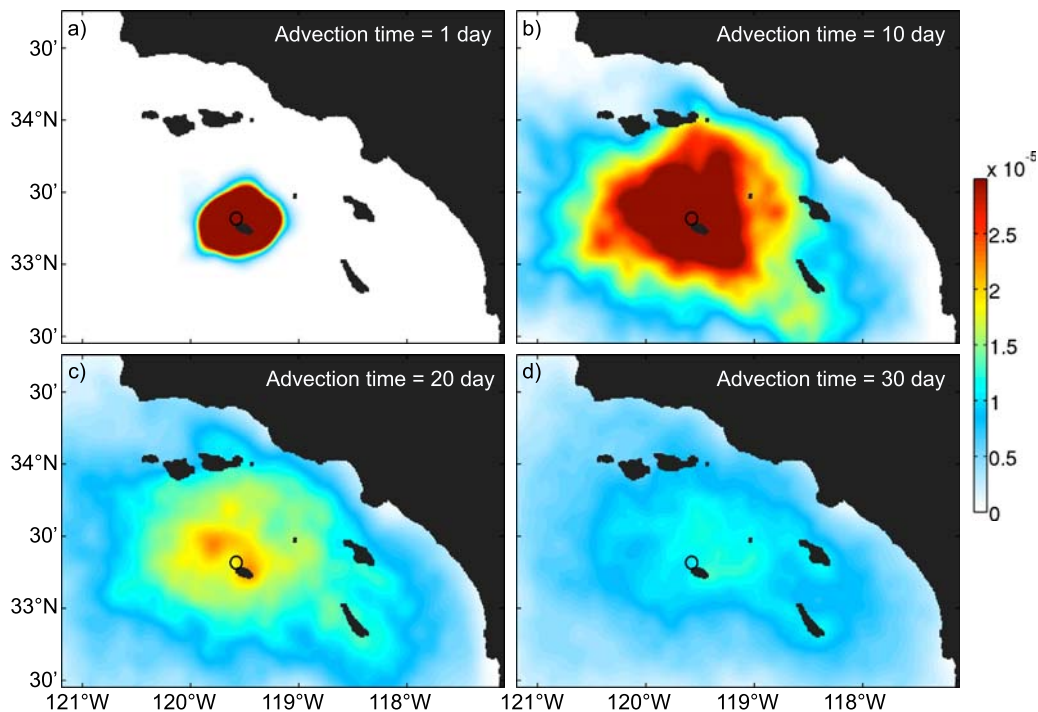


Figure 3. Lagrangian probability density functions (Lagrangian PDFs) from the site on the shore of San Nicholas Island (black circles; site 130) for the advection time of (a) 1 day, (b) 10 days, (c) 20 days, and (d) 30 days. The Lagrangian PDFs are computed through equations (3)–(5), given all Lagrangian particle trajectories, regardless of the release season and year. Colors indicate the probability density of a particle location for a given advection time in km^{-2} .

(Figure 2c). However, many of those released just two weeks later (15 February 1996; Figure 2d), are transported poleward along the mainland coast and are found within the SB Channel after 30 days. Differences in the release times of just two weeks can lead to very different dispersal patterns. This clearly illustrates the characteristics of a turbulent dispersion problem.

[17] Lagrangian length and timescales as well as values of eddy diffusivity are estimated to validate the simulated dispersal patterns. These are compared with similar statistics obtained from surface drifter observations for a 5° by 5° box centered at 35°N 120°W [Swenson and Niiler, 1996]. We employ the definition of eddy diffusivity proposed by Davis [1987] following the approach of Swenson and Niiler [1996]. We find Lagrangian time and length scales of 3.6 ± 0.8 days and 32.2 ± 7.1 km, respectively, that correspond to an eddy diffusivity of $3.6 \pm 1.0 \times 10^7 \text{ cm}^2 \text{ s}^{-1}$. Here the numbers after \pm indicate the standard deviation among release sites. Swenson and Niiler [1996] found typical values for the Lagrangian time and length scales of 1.8–6.8 days and 16–64 km, respectively, while for the eddy diffusivity, $1.7\text{--}7.0 \times 10^7 \text{ cm}^2 \text{ s}^{-1}$. There is good correspondence between Lagrangian statistics obtained from the simulation and the analysis of field observations, strengthening our confidence in our simulated dispersal patterns.

[18] The Lagrangian PDF statistically describes the expected locations of water particles that are released from a single site and transported over a given time interval. For example, the Lagrangian PDF from a site on San Nicholas Island (site 130) calculated using 7 years of trajectories (1996–2002) is shown in Figure 3. Determinations of the

Lagrangian PDF from this site are roughly isotropic and they become more homogenous as the advection time becomes longer (Figure 3). Water parcels from this site can reach nearly all of the SCB within 20 days (Figure 3c). For an advection time of 10 days, strong connectivity patterns are expected to sites on the south side of Anacapa and Santa Cruz Islands, but not on the mainland or Northern Islands (Figure 3b). For longer advection times, similar levels of connectivity are expected throughout the SCB (Figure 3d).

3.2. Release-Position Dependence of Expected Dispersal Patterns

[19] The San Nicholas Island source site (#130; Figure 1a) is relatively isolated from the other Channel Islands and the mainland. Lagrangian particle transport is, therefore, less influenced by the complex coastal topography and distinctive circulation patterns of the SBC, resulting in a roughly isotropic Lagrangian PDF (Figure 3). Lagrangian PDFs for releases from other sites, however, show a strong directionality associated with complex coastline and bathymetry of the SCB (Figure 4).

[20] Simulated mean dispersal patterns can be categorized into four groups, depending on the release-site location. First, Lagrangian particles released on the mainland sites show distinctive nearly unidirectional mean dispersal patterns (Figures 4a–4d). The mean poleward transport is observed from sites between the international border and Ventura (site 45), but not from sites in the north of Ventura (Figures 4e–4f). Second, Lagrangian particles released from sites within the SB Channel tend to stay within the

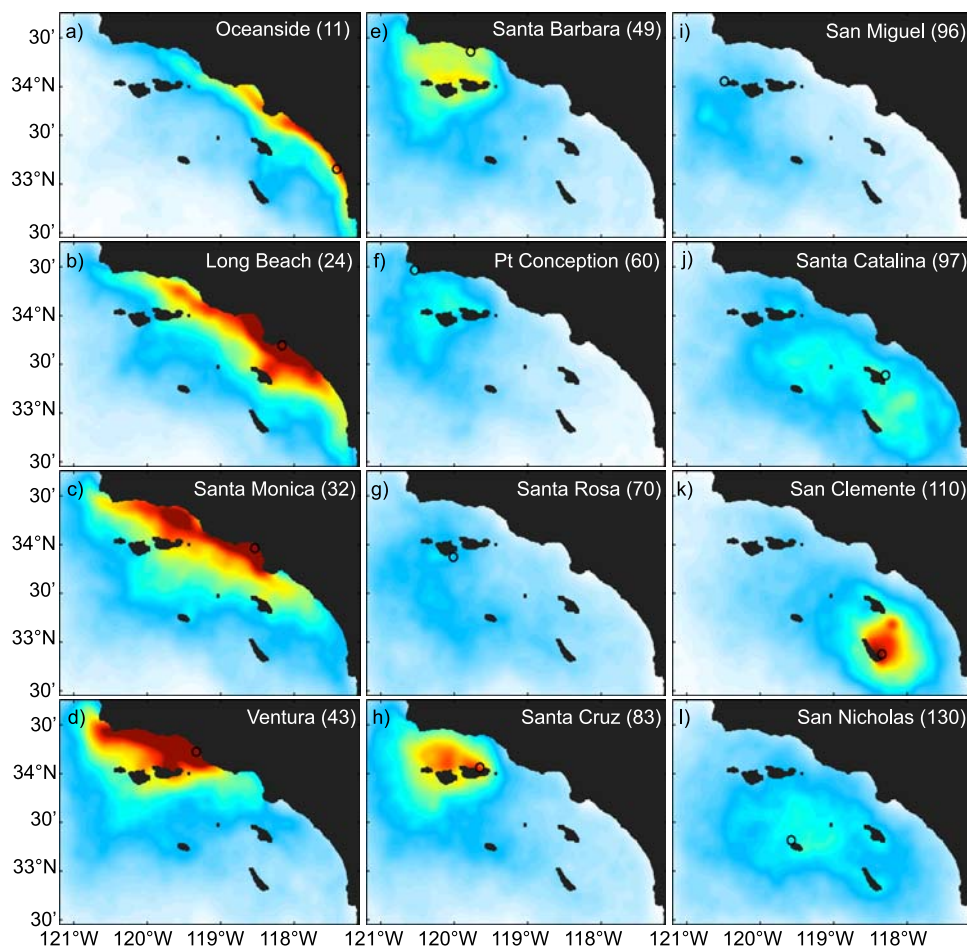


Figure 4. Lagrangian probability density functions (Lagrangian PDFs) for the advection time of 30 days from 12 different sites: (a) Oceanside (11), (b) Long Beach (24), (c) Santa Monica (32), (d) Ventura (43), (e) Santa Barbara (49), (f) Point Conception (58), (g) Santa Rosa Island (70), (h) Santa Cruz Island (83), (i) San Miguel Island (96), (j) Santa Catalina Island (97), (k) San Clemente Island (110), and (l) San Nicholas Island (130), where the numbers in the parentheses indicate the site numbers (Figure 1). For a detailed description of Lagrangian PDFs see the caption of Figure 3. The color scale is shown in Figure 3.

Channel (Figures 4e and 4h). Particles released from the outer edge of the SB Channel do not show this retention (Figures 4f and 4i). Third, water parcels originating in the Southern Channel Islands tend to stay in the southeastern part of the Bight (Figures 4k and 4l). This retention signal is strongest on the eastern shore of San Clemente Island (Figure 4k), and becomes weaker far from this site (Figures 4j and 4l). The final group is less affected by complex topography and distinctive circulation patterns, and do not exhibit strong spatial structures (Figures 4f, 4g, 4i, 4j and 4l).

[21] The position dependence of Lagrangian PDFs reflects the distinctive circulation patterns of the SCB [e.g., *Sverdrup and Fleming*, 1941; *Lynn and Simpson*, 1987; *Hickey*, 1992, 1993; *Dong et al.*, 2009]. Strong and persistent equatorward winds along the central California coast, driving the California Current throughout the year, separate from the coast in the vicinity of Point Conception, leaving the winds in the SCB, in general, weak and highly variable [e.g., *Winant and Dorman*, 1997]. This wind-sheltering, combined with a poleward pressure gradient, creates the Southern California Countercurrent (SCC [e.g., *Hickey*, 1979; *Lynn*

and Simpson, 1987]). This SCC can be found throughout the SBC and can exit at Point Conception [e.g., *Lynn and Simpson*, 1987]. Lagrangian PDFs for mainland release location (Figures 4a–4d) clearly reflect the SCC. The juxtaposition of the California Current offshore the bight and SCC inside forms a cyclonic circulation pattern (Southern California Eddy) that is roughly fixed at the shallow offshore banks of the SCB [Bernstein et al., 1977; *Lynn and Simpson*, 1987]. The California Current has a large shoreward component just in the south of the international boarder, and the part of the current flows northward as the nearshore limb of SCC, creating cyclonic circulation between the islands Santa Catalina and San Clemente (hereafter the Catalina-Clemente Eddy) [e.g., *Lynn and Simpson*, 1987]. Similarly, a smaller cyclonic circulation is observed in the western part of the SB Channel (hereafter the SB-Channel Eddy), bounded by Northern Channel Islands [e.g., *Harms and Winant*, 1998; *Beckenbach and Washburn*, 2004; *Nishimoto and Washburn*, 2002]. Retention of particles (Figures 4e, 4h and 4k) coincide with the location of this cyclonic circulation.

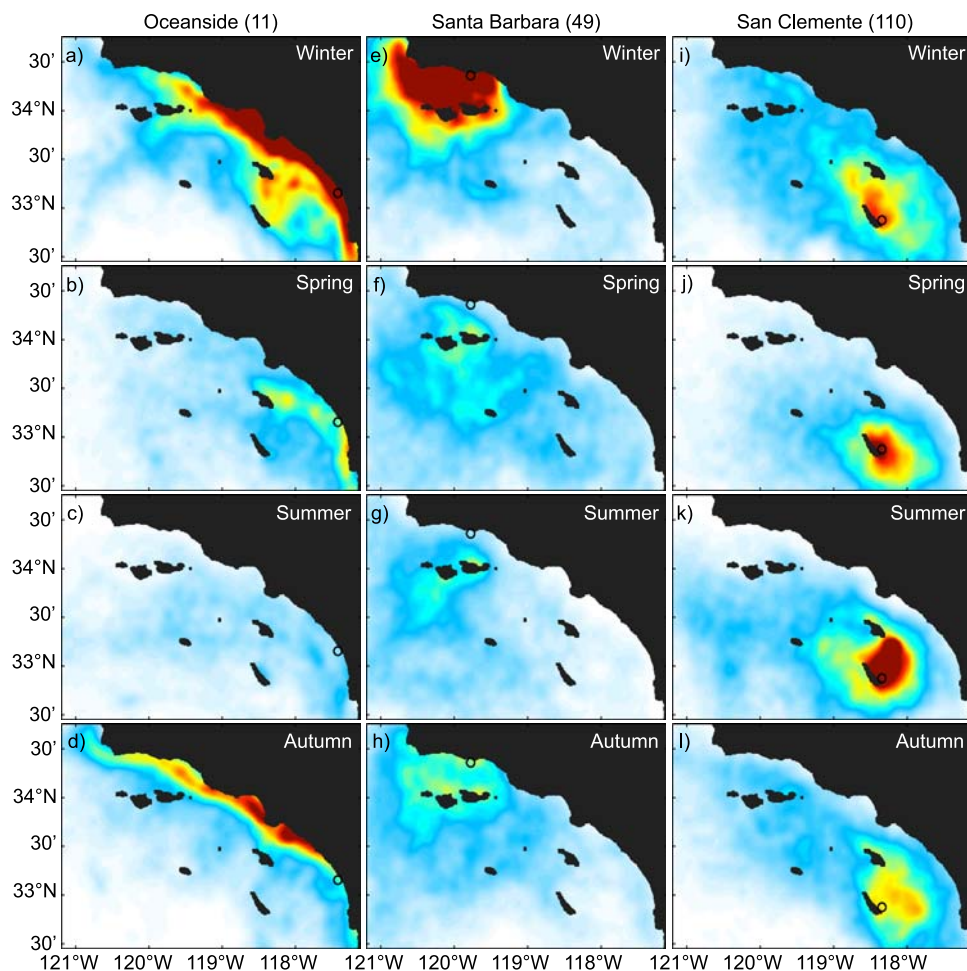


Figure 5. Seasonal variability in Lagrangian probability density functions (Lagrangian PDFs). Lagrangian PDFs from a site on the shore of (a–d) Oceanside (site 11), (e–h) Santa Barbara (site 49), and (g–l) San Clemente Island (site 110) conditioned upon the Lagrangian particle release season: (top row) winter, (second row) spring, (third row) summer, and (bottom row) autumn are shown. The black circles indicate the release site locations. For a detailed description of Lagrangian PDFs, see the caption of Figure 3. The color scale is also found in Figure 3.

[22] Within the SB Channel, Lagrangian PDFs show the highest value at Chinese Harbor (site 83) on the northeastern side of Santa Cruz Island. This is where surface-drifters deployed in the SBC often run aground [e.g., *Winant et al.*, 1999]. These high PDF values are not caused by the beaching of particles as only 0.2% of the released water parcels ran aground.

3.3. Seasonal and Interannual Variability of Expected Dispersal Patterns

[23] Circulation patterns in the SCB show strong seasonality, driven by variability in wind-forcing and alongshore pressure gradients [*Lynn and Simpson*, 1987; *Di Lorenzo*, 2003]. During winter, the wind stress within the bight is weaker, spatially homogeneous and temporally variable; during summer, the wind-forcing is stronger and more persistent with large spatial gradients [*Winant and Dorman*, 1997; *Dong et al.*, 2009]. The core of the California Current is strongest in spring and summer, and tends to be closer inshore [*Bograd et al.*, 2000]. The juxtaposition of the California Current and SCC (and the Southern California

Eddy) becomes much more coherent in summer [*Lynn and Simpson*, 1987]. Although the flow in the SCB is mostly poleward throughout the year, equatorward flow does occur at the coast near Oceanside (CalCOFI line 90) in the summer and weaker in the spring [e.g., *Lynn and Simpson*, 1987]. Seasonality of the circulation in the SBC can be characterized by differing synoptic circulation states responding to differing wind and pressure fields – upwelling and eastward flow in spring, a strong cyclonic circulation in summer, poleward relaxation in fall, and weak and variable circulation in winter [e.g., *Bray et al.*, 1999; *Winant et al.*, 1999].

[24] Expected 30-day dispersal patterns show strong seasonality reflecting known seasonal changes in the circulation of the SBC (Figure 5). First, poleward transport along the mainland shows dramatic seasonality (Figures 5a–5d). The mean poleward transport from Oceanside (site 11) is prominent in winter and autumn (Figures 5a and 5d), while it almost disappears in the spring and summer seasons (Figures 5b and 5c). The mean poleward transport is less coherent in winter than in autumn (see Figures 5a and 5d),

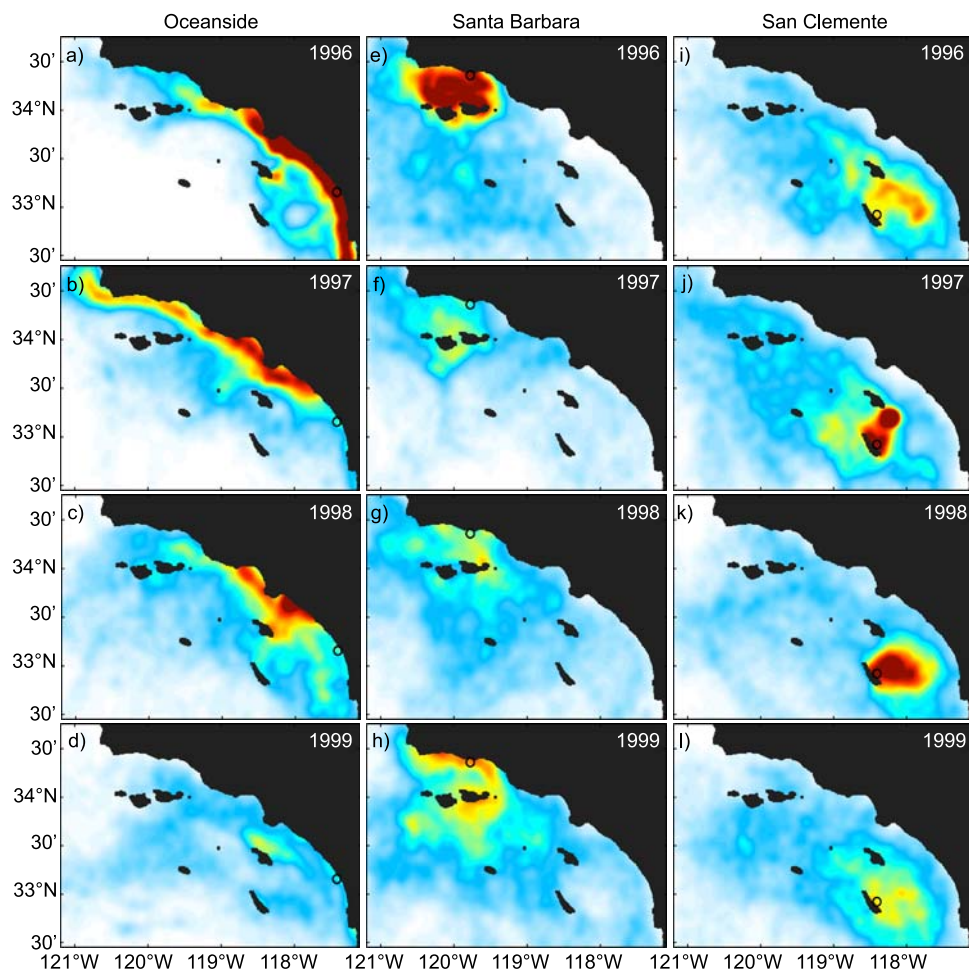


Figure 6. Interannual variability in Lagrangian probability density functions (Lagrangian PDFs). Lagrangian PDFs from a site on the shore of (a–d) Oceanside (site 11), (e–h) Santa Barbara (site 49), and (g–l) San Clemente Island (site 110) conditioned upon the Lagrangian particle release year: (top row) 1996, (second row) 1997, (third row) 1998, and (bottom row) 1999 are shown. The black circles indicate the release site locations. For a detailed description of Lagrangian PDFs, see the caption of Figure 3. The color scale is also found in Figure 3.

because of the temporally variable wind-forcing in winter. Second, regional retention in the SB Channel is dominant in winter, while this signal is hardly seen in other seasons (Figures 5e–5h) when upwelling and eastward flow dominates [e.g., *Dever et al.*, 1998; *Winant et al.*, 1999]. This implies that Lagrangian particles tend to stay in the Channel simply because the particle transport is limited due to weak and variable flows, and not because SB cyclonic eddy retains particles [e.g., *Nishimoto and Washburn*, 2002]. Finally, regional retention of Lagrangian particles off the eastern shore of San Clemente Island shows much less seasonal variability (Figures 5i–5l) than is observed for the other retention zones shown here (Figures 5a–5h). The retention off San Clemente Island is consistently seen throughout all seasons (Figure 5), showing only moderate seasonal variability.

[25] Strong interannual changes in the circulation of the SCB are punctuated by the El Niño event of 1997 to 1998 and the rapid transition to La Niña conditions in 1998 and 1999 [*Bograd et al.*, 2000; *Schwing et al.*, 2000; *Lynn and Bograd*, 2002]. The 1997–1998 El Niño is characterized by

a significant increase in dynamic height and a strengthening and broadening of the poleward nearshore flow, starting the late spring of 1997 and ending the summer of 1998. By early 1999, the regional circulation features reversed as strong sustained upwelling-favorable winds occurred through late 1998 and much of 1999, resulting in greater than usual southward transport by the California Current [e.g., *Schwing et al.*, 2000].

[26] The expected 30-day dispersal patterns represent well the expected interannual variability (Figure 6). The mean poleward transport of Lagrangian particles along the mainland is substantially stronger in 1997, reflecting enhanced SCC during the El Niño event (Figure 6b). The annual mean poleward transport almost diminishes in 1999, due to an enhanced California Current during the La Niña event (Figure 6d). The Lagrangian PDF for 1998 reflects both climatic anomalies as El Niño conditions were still found during the late winter months while the La Niña event started during the fall (Figure 6c). Retention in the SB Channel, caused by weak and variable circulation in the winter, is not seen during the El Niño event (Figure 6f) and is

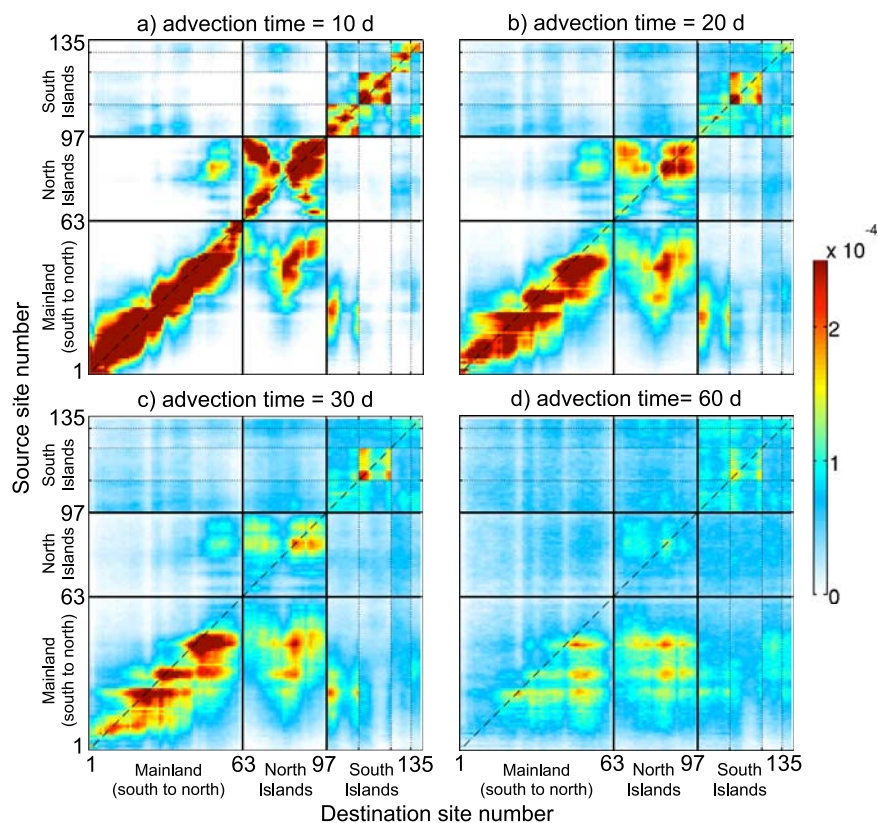


Figure 7. Mean coastal connectivity for the advection time of (a) 10 days, (b) 20 days, (c) 30 days, and (d) 60 days. The mean connectivity for a given source site j (horizontal axis) and destination site i (vertical axis) is determined by evaluating the Lagrangian probability density functions (e.g., Figures 3 and 4) for the location of site j and site i , as described by equation (7). For comparison, connectivity values are normalized so that the summation of the mean connectivity over all possible combinations becomes one. All Lagrangian particles released from all sites from 1 January 1996 through 31 December 2002 are accounted for in computing connectivity. The black dashed line indicates self connectivity, i.e., the source and destination sites are identical. The solid lines define three regions: the mainland (sites 1–62), Northern Channel Islands (sites 63–96), and Southern Channel Islands (sites 97–135).

reduced for La Niña periods (Figure 6h). The retentive nature of the SB Channel is greatest during 1996, which is a “normal” year (Figure 6e). During an El Niño (La Niña) event, the relaxation (upwelling) circulation state is enhanced and poleward (equatorward) flow becomes stronger. For either case, more Lagrangian particles are exported from the SB Channel (Figures 6f–6h). This result is consistent with the analysis of remote observations of phytoplankton chlorophyll concentrations in the SB Channel which show high concentrations during “normal” years compared with the El Niño or La Niña years [Otero and Siegel, 2004]. Retention features off the eastern shore of the San Clemente Island are relatively insensitive to the year of evaluation (Figures 6i–6l) although retention appears to be more substantial during the El Niño (Figures 6j and 6k).

4. Coastal Connectivity of the Southern California Bight

4.1. Quantifying Connectivity Matrices

[27] Coastal connectivity can be quantified by evaluating the simulated Lagrangian PDFs for a given source and a given destination (equation (7)) and is most readily expressed

in matrix form. The connectivity matrix illustrates the degree of connectivity for the possible combinations of nearshore sites given an advection timescale (Figure 7). For a short advection time (10 days), strong connectivity is found mostly for nearby sites (Figure 7a). The mainland, Northern Channel Islands and Southern Channel Islands are, in general, not well connected with each other for these advection times, although there are some exceptions [e.g., transport from Santa Barbara (site 49) to Chinese Harbor (site 83)]. On the other hand, the connectivity matrix becomes more homogeneous for a relatively long advection time (60 days; Figure 7d), implying that most nearshore sites have a more uniform probability of being affected by any other site (Figure 7d). Accordingly, the coefficient of variation (CV; the ratio of a standard deviation to a mean) for the degree of mean connectivity among different sites changes as $CV = 2.05, 1.12, 0.79$ and 0.44 as the advection time increases as $\tau = 10, 20, 30$ and 60 days. For intermediate advection times (20 to 30 days), coastal connectivity is not homogeneous, reflecting distinctive circulation patterns of the SCB (Figures 7b and 7c). Further for advection times of 20 days and longer, the calculated connectivity matrices are asymmetric (Figures 7b–7d). This

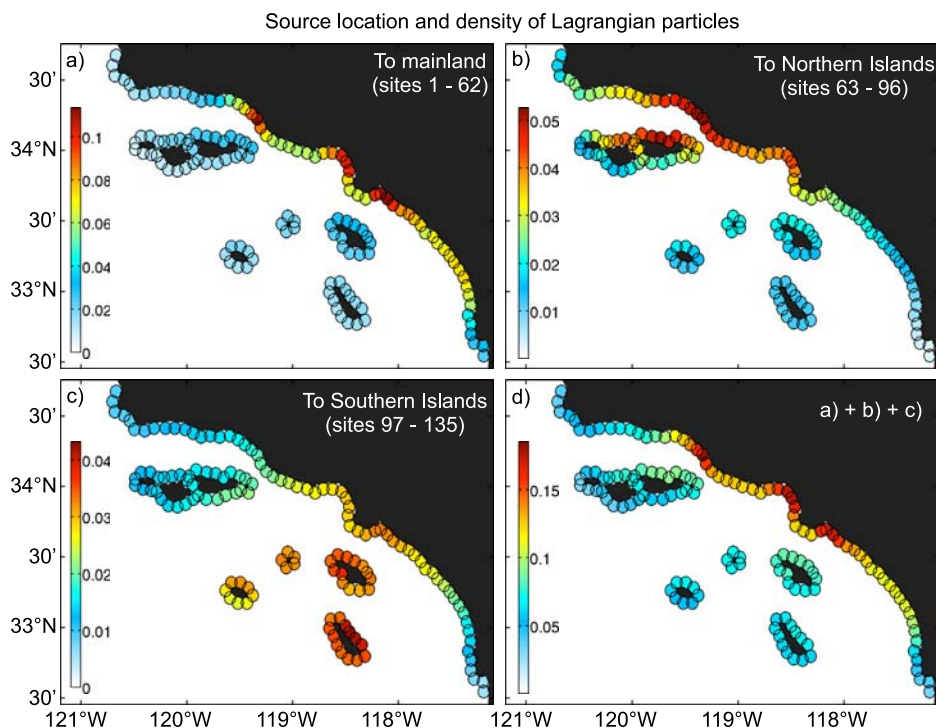


Figure 8. The source location and density (source strength) of Lagrangian particles that are transported to (a) the mainland (sites 1–62), (b) the Northern Channel Islands (sites 63–96), (c) the Southern Channel Islands (sites 97–135), and (d) all sites (sites 1–135) for the advection time of 30 days. For example, (a) a value of 0.1 indicates that 10% of Lagrangian particles that were released from this site were found somewhere along the mainland after 30 days. The source strength is determined by taking a partial summation of the mean connectivity (see Figure 7) for given destination sites (equation (9)). All Lagrangian particles released from 31 January 1996 through 31 December 2002 are used to compute the source strength. Different color scales are applied for each panel to show the spatial patterns effectively.

implies that the direction of the connection among sites is important beyond just knowing the distance between sites (as would occur in a purely diffusive environment).

4.2. Source and Destination Strength Distributions

[28] Spatial distributions of the source and destination strengths (equations (8) and (9)) provide a regional illustration of much of the information provided in the connectivity matrix. Source strength distributions for particles that are successfully transported to the mainland sites (Figure 8a), to the Northern Channel Islands (Figure 8b), the Southern Channel Islands (Figure 8c) or to any nearshore site within the domain (Figure 8d) can be constructed by summing the connectivity matrix over the proper destination sites. Similarly by summing over appropriate source sites, the distribution of destination strengths from the mainland, Northern Island, Southern Islands and from all sites can be visualized (Figure 9). For both of these summaries, the advection time is set to 30 days. Also, note that the color bars for the four panels in Figures 8 and 9 differ.

[29] Source strength distributions show that water parcels with destinations on the mainland, the Northern Channel Islands or the Southern Channel Islands all have distinct source locations (Figures 8a–8c). Water parcels arriving at the Northern Channel Islands originate mostly from the northern portion of the mainland coast (i.e., between Santa Barbara and Santa Monica Bay) and the northern shore of

the Santa Cruz and Santa Rosa Islands (Figure 8b). On the other hand, water parcels arriving at the Southern Channel Islands come mainly from those islands and the mainland centered around Palos Verdes Peninsula (Figure 8c).

[30] Water parcels arriving at the mainland sites have come mainly from the mainland and not from the offshore Islands (Figure 8a). Source strengths are greater between Oceanside and Ventura and peaks near three sites (i.e., Long Beach [24], Santa Monica [32] and Ventura [43]; Figure 8a) as can also be seen in the connectivity matrix (Figure 7c). Although many water parcels released from these sites are transported poleward alongshore, a substantial fraction of the water parcels are retained locally (Figure 7c). Accounting for water parcels to all sites, sites around Ventura, Santa Monica and Long Beach are the strongest sources because these sites export water parcels not only to mainland sites, but also to the Channel Islands (see Figures 4b–4d and Figure 8d). Overall, the mainland sites are good sources, while the Island sites are poor sources, although there is substantial transport of water parcels from the mainland sites.

[31] Destination strength distribution shows regional retention of water parcels for both the Northern and Southern Channel Islands while the mainland receives many fewer water parcels (Figures 9a–9c). Unlike the source strength distribution (Figures 8a–8c), destination strengths from the mainland, Northern and Southern Channel Islands are

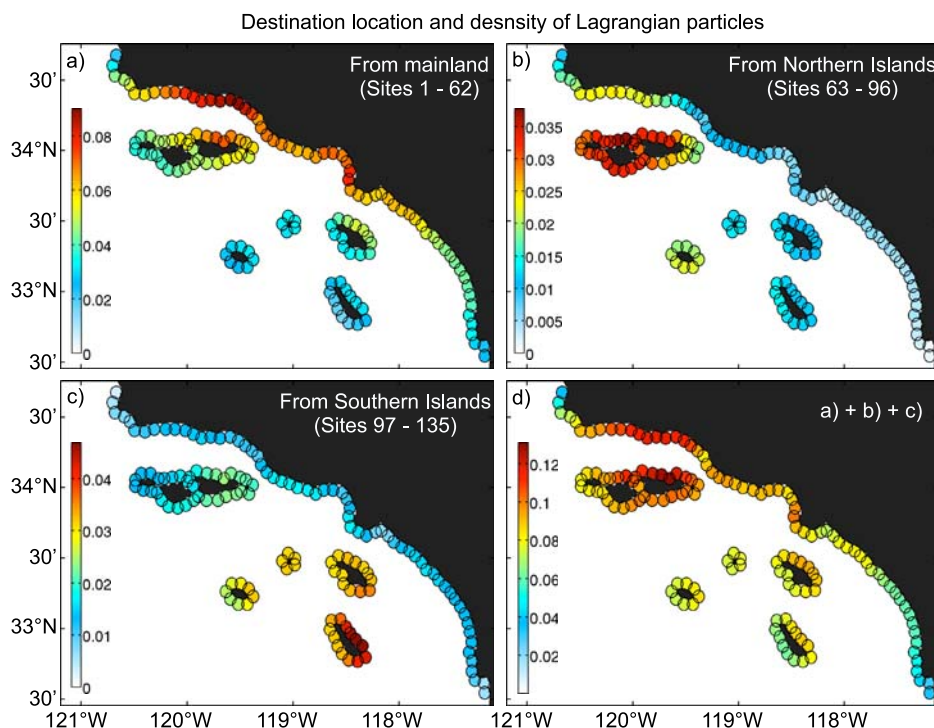


Figure 9. The destination location and density (destination strength) of Lagrangian particles that are transported from (a) the mainland (sites 1–62), (b) the Northern Channel Islands (sites 63–96), (c) the Southern Channel Islands (sites 97–135), and (d) all sites (sites 1–135) for the advection time of 30 days. The destination strength is determined by taking a partial summation of the mean connectivity matrix (see Figure 7) for given source sites (equation (8)). All Lagrangian particles, regardless of the release season and year, are used to compute the destination strength.

roughly comparable (Figures 9a–9c). Accounting for all water parcels from all sites, Chinese Harbor (northeastern shore of Santa Cruz Island; site 83) attracts the most water parcels (Figure 9d), collecting water parcels from the mainland due to poleward transport (Figures 4b–4d) and from the sites within the SB Channel (both on the mainland and Northern Channel Islands) due to local retention (Figures 4e and 4h). This is consistent with the location of beached drifters from deployments in the SB Channel [Winant *et al.*, 1999].

[32] The modeled dispersal patterns differ by season (Figure 5) and by year (Figure 6) which will obviously have an influence on the source strength distributions evaluated either by season (Figure 10) or by year (Figure 11). Source strength distributions of particles that are advected to the Northern Channel Islands change dramatically from season to season (Figures 10a–10d). In winter, water parcels reach the Northern Channel Islands from a wide range of source locations including the Southern Channel Islands (Figure 10a). In spring and summer, the strong sources weaken and become more local to the SB Channel (Figures 10b–10c). In autumn, strong sources are found mostly along the central mainland coast (Figure 10d). Source distributions to the Southern Channel Islands change less substantially from season to season (Figures 10e–10h). Source strength distributions for particles advected to the Southern Channel Islands (Figure 10) are similar to the mean source distributions (Figure 8c), while transport from the mainland becomes substantially less in autumn (Figure 10h). Destination strength distributions for particles advected from

the mainland directly corresponds to the seasonal cycle of poleward transport (Figures 5i–5l).

[33] Interannual changes in the spatial distribution of particle source strengths are less apparent (Figure 11). For example, source strengths (to the Northern Channel Islands or from the mainland) are only slightly weaker in El Niño year (1997; Figures 11b and 11j) than in the normal year (1996; Figures 11a and 11i). However, these differences are much smaller than the magnitudes of the observed seasonal changes in source strength (Figure 10). For water parcels advected to the Southern Channel Islands, regional connectivity patterns differ for 1997 where San Clemente Island is a strong and isolated source (Figure 11f) which differs from the other years which shows a substantial mainland source (Figures 11e, 11g and 11h). Changes in the destination strengths, from the mainland, in 1999 become substantially weaker, although the spatial pattern is nearly unchanged (Figures 11i–11l).

4.3. Assessing the Time Scales of Coastal Connectivity

[34] The above analyses of coastal connectivity have shown the temporal dependence of connectivity patterns and strengths as a function of advection time (Figure 7), season (Figure 10), and year (Figure 11) of evaluation. However, individual dispersal patterns include intrinsic variability, reflecting water parcel transport by coastal eddy motions (Figure 2). Clearly, these intraseasonal eddy motions must contribute some to coastal connectivity. Monthly time series of connectivity strength between six pairs of nearshore sites are shown in Figure 12 for sites with

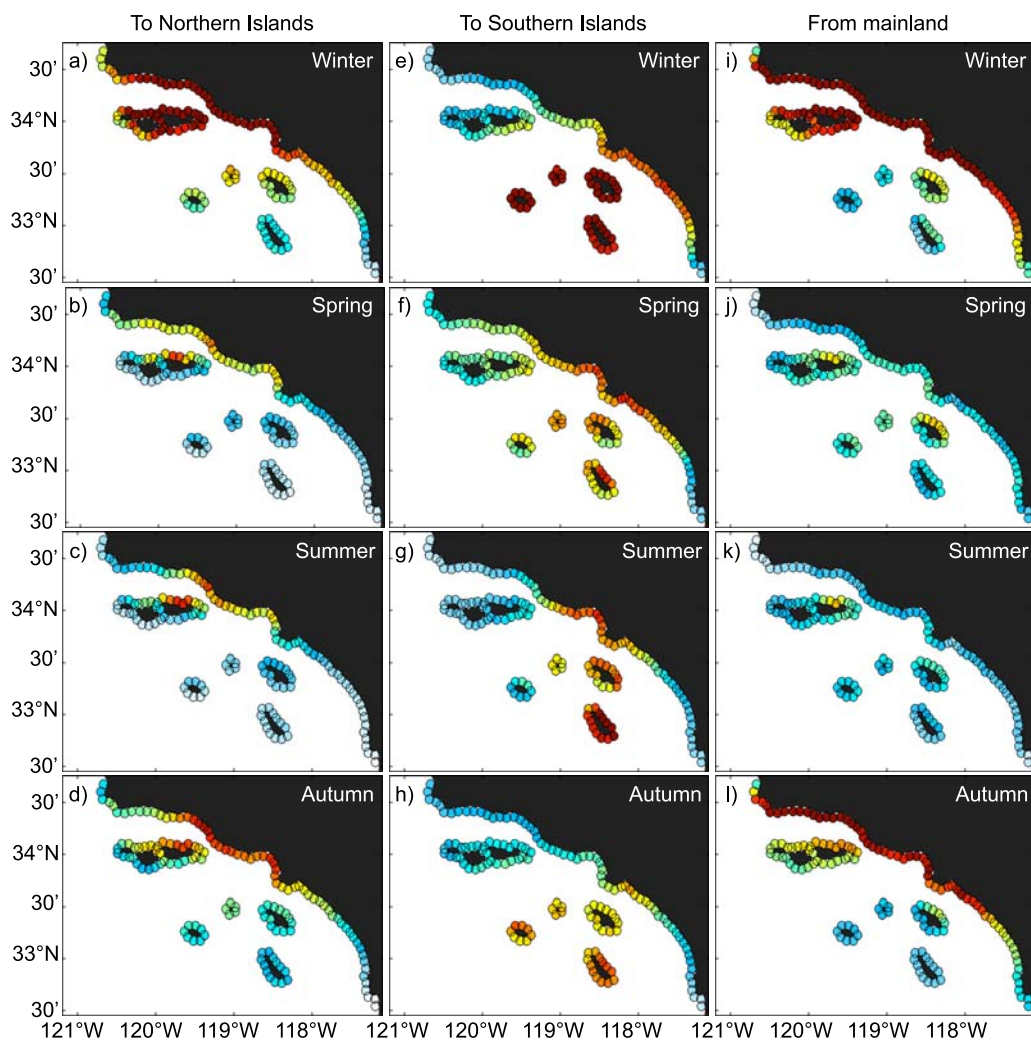


Figure 10. Seasonal variability in regional mean connectivity for the advection time of 30 days. Source strength to (a–d) the Northern Channel Islands (sites 63–96) and (e–h) the Southern Channel Islands (sites 97–135) and (i–l) destination strength from the mainland (sites 1–62) and are shown, conditioned upon the particle-release season: (first rows) winter, (second rows) spring, (third rows) summer, and (fourth rows) autumn. The color scales for the panels (a–d), (e–h), and (i–l) are shown in Figures 8b, 8c and 9a, respectively.

strong mean connectivity (Figures 12a and 12b), between sites with themselves (Figures 12c and 12d), and sites with weak mean connectivity (Figures 12e and 12f). Connectivity is clearly not persistent even within a season. There is a strong intraseasonal variability. This intrinsic variability of connectivity is not an artifact caused by an insufficient number of particles released in the simulated flow fields as connectivity patterns determined with twice of the number of particles released resulted in nearly identical dispersal patterns (not shown). Hence the intraseasonal peaks in coastal connectivity are created by the transient threads of connections created by coastal eddying motions [e.g., Siegel *et al.*, 2008].

[35] In order to understand the role of timescales on connectivity patterns, we first partition the connectivity matrix into a time mean and a standard deviation which measures the time variability on all scales (Figures 13a and 13b). Here we computed the mean and standard deviations from the monthly connectivity time series

(e.g., Figure 12). Mean connectivity levels are substantially less than those for time variable connections as measured by the standard deviation distribution.

[36] The time variable components of connectivity have sources due to seasonal and interannual variations in circulation patterns as well as eddy-induced water parcel transports. Here we quantify the degree of each source of variability by filtering the connectivity time series (Figure 10) and calculating the root mean variance in the interannual and seasonal time band (Fourier modes with the time period of 6 months or longer; Figure 13c) and for the intraseasonal band (Fourier modes with the time period less than 6 months; Figure 13d). The Fourier analysis shows that intraseasonal band has roughly the same power as the seasonal and interannual bands combined (Figures 13c and 13d). Further, the seasonal and interannual connectivity (Figure 13c) and the eddy timescale connectivity (Figure 13d) are each comparable to the magnitude of the mean connectivity pattern (Figure 13a). This result suggests that eddy-

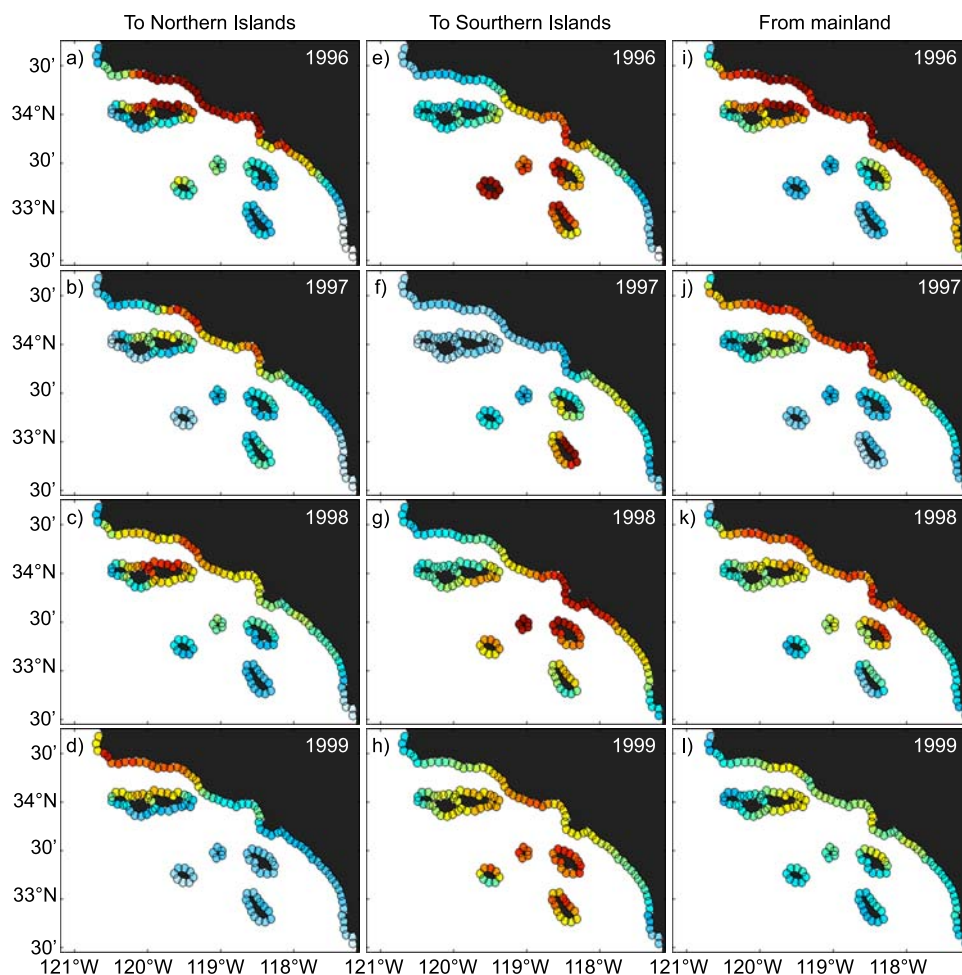


Figure 11. Interannual variability in regional connectivity for the advection time of 30 days. Source strength to (a–e) the Northern Channel Islands (sites 63–96) and (f–h) the Southern Channel Islands (sites 97–135) and (i–l) destination strength from the mainland (sites 1–63) are shown, conditioned upon the particle-release year: (first rows) 1996, (second rows) 1997, (third rows) 1998, and (fourth rows) 1999. The color scales for the panels (a–d), (e–h), and (i–l) are shown in Figures 8b, 8c and 9a, respectively.

induced variability has a power to greatly control connectivity patterns [Siegel *et al.*, 2008].

5. Discussion

[37] We assessed coastal connectivity in the Southern California Bight (SCB) by numerically simulating the trajectories of millions of Lagrangian particles using a Lagrangian PDF formulation. The results showed good qualitative agreement with previous descriptions of circulation of the SCB for available observational syntheses. The quantification of coastal connectivity is also useful for marine resource management applications. In the following we address the validity of the modeling approaches and demonstrate how to use this quantification of coastal connectivity in resource management.

5.1. Model Assessment

[38] The simulated connectivity patterns for the SCB are dependent upon the skill of the ocean circulation model and the appropriateness of the Lagrangian calculations. Out-

standing issues to be considered here include the degree at which the Dong and McWilliams [2007] model simulations represent actual ocean flows, the importance of subgrid scale motions on the simulated Lagrangian motions and the effects of domain size on the regional assessment of connectivity.

[39] Dong *et al.* [2009] assessed the simulation outputs against extensive observational data, including High-Frequency (HF) radar data, current meters, Acoustic Doppler Current Profilers (ADCP) data, hydrographic measurements, tide gauges, drifters, and altimeters. For example, the ROMS solution reproduces the SB Channel Eddy having a good agreement with current meters and drifter observations of the Mineral Management Service (MMS) and of the HF radar data [e.g., Nishimoto and Washburn, 2002]. The difference in the seasonal mean currents is within 10–20 % from the HF radar data. The mean and variations of the model currents show similar patterns with ADCP buoys in the SCB from the National Buoy Data Center (46023, 46053, 46054, 46047 and 46048), four ADCP moorings supported by MMS and nine ADCP

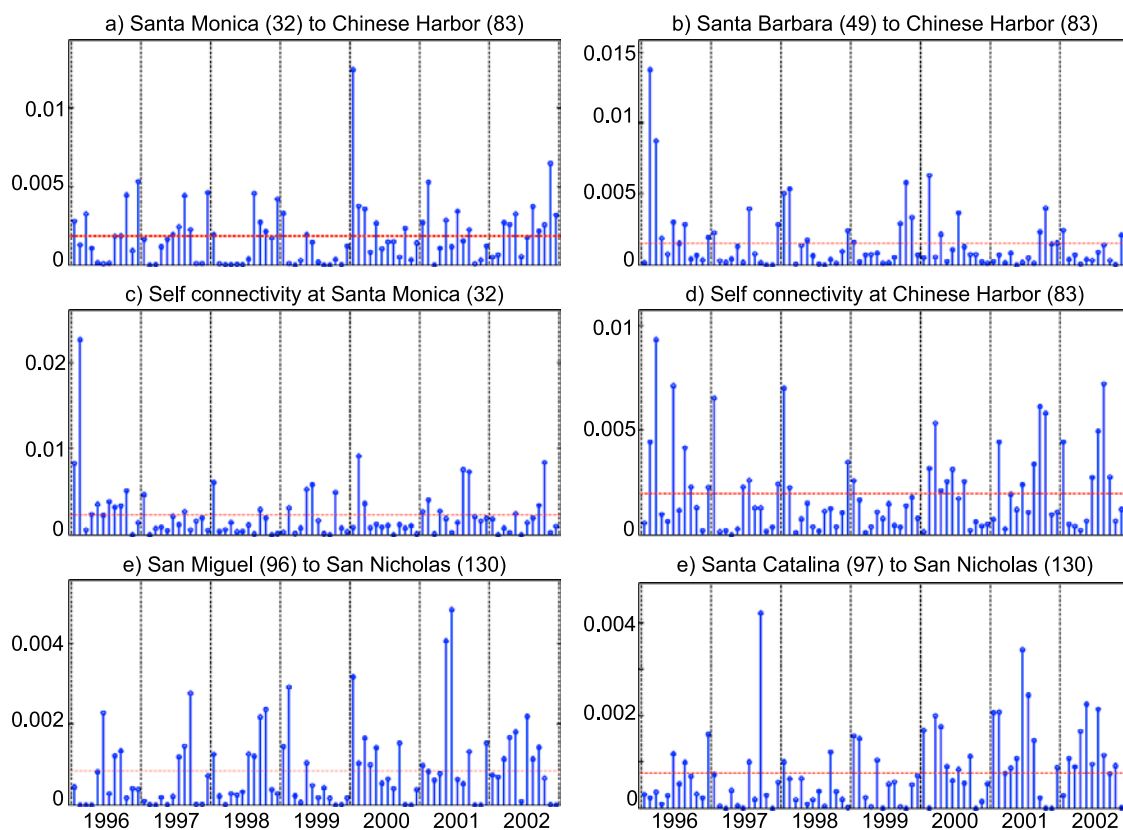


Figure 12. Time series of monthly connectivity between a given source site j and a given destination site i for the advection time of 30 days. The bars indicate the probability for the event that a particle released from site j in a particular month of a particular year are transported to site i . The red line indicates the mean connectivity. Panels indicate connectivity (a) from Santa Barbara (49) to Santa Cruz Island (83), (b) from Ventura (43) to Santa Cruz Island (83), (c) from Santa Monica (32) to itself, (d) from Santa Cruz Island (83) to itself, (e) from San Miguel Island (96) to San Nicholas Island (130) and (f) from Santa Catalina Island (97) to San Nicholas Island (130). The numbers in the parentheses indicate the site numbers (see Figure 1).

moorings deployed by Los Angeles County Sanitation District except those close to the open boundaries (46047 and 46048). The mean differences are at the level of several cm s^{-1} or tens of percent of the signal, and the standard deviation ratio is within a few tens of percent of unity. The magnitudes and structural patterns (such as thermocline and thermohaline depth) of temperature and salinity from ROMS and the California Cooperative Oceanic Fisheries and Investigations (CalCOFI) data agree fairly well each other, within about $1\text{--}2^\circ\text{C}$ and 0.2 psu, respectively. A comparison of the temperature time series at three MMS stations in the SB Channel [Lynn and Bograd, 2002; Dever and Winant, 2002] with the ROMS simulation shows that the temperature increases dramatically in late 1997 through early 1998 with almost the same magnitude and timing. Further detailed analysis against more observations can be found in Dong *et al.* [2009]. Comparisons with observational data reveal that ROMS reproduces a realistic mean state of the SCB oceanic circulation, as well as its interannual and seasonal variability.

[40] One way to further validate the model connectivity is through quantitative Lagrangian validations. As the first step, we computed Lagrangian time and length scales and eddy diffusivities, and found a reasonable agreement with

observations of Swenson and Niiler [1996], as mentioned above. This agreement supports the ROMS model in describing mesoscale eddy motions.

[41] The neglect of diffusion by subgrid-scale motions in Lagrangian trajectory calculations can lead to underestimation of the scales of dispersal. Values of eddy diffusivity scale as $u^2 l$, where l is the scale of motion and u^2 is twice its kinetic energy. Lagrangian time and length scales for the present simulations are 3.6 ± 0.8 days and 32.2 ± 7.1 km, respectively and correspond to an eddy diffusivity of $3.6 \pm 1.0 \times 10^7 \text{ cm}^2 \text{ s}^{-1}$. Both the u^2 and l associated with subgrid-scale eddies are much smaller than those of mesoscale motions. Values of subgrid-scale eddy diffusivity, for instance, can be quantified by using the Smagorinsky model [Smagorinsky, 1993] as

$$\gamma_t = (C_s \Delta_G)^2 \sqrt{\langle S_{ij} \rangle_t \langle S_{ij} \rangle_t} \quad (10)$$

where Δ_G is the grid scale, C_s is an empirical constant, and $\langle S_{ij} \rangle_t$ is resolved strain rate tensor. Maximum values of the horizontal strain rate in the SBC are close to Coriolis frequency $f = 7.7 \times 10^5 \text{ s}^{-1}$ [Beckenbach and Washburn, 2004; Dong and McWilliams, 2007]. Given $C_s = 0.2$ and

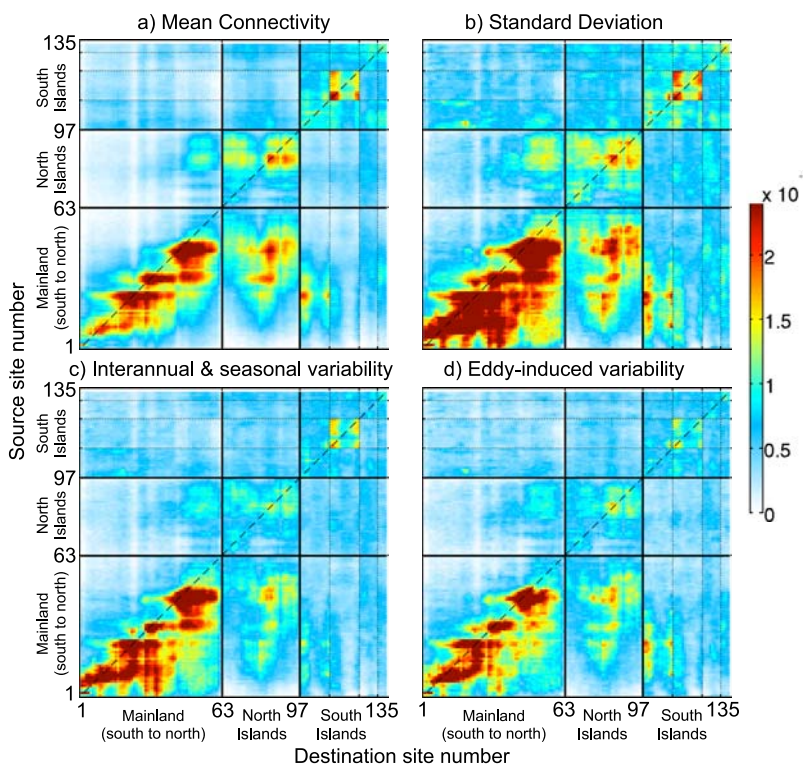


Figure 13. (a) Mean, (b) standard deviation, (c) interannual/seasonal variability, and (d) eddy-induced variability of realized monthly coastal-connectivity (see Figure 12) for the advection time of 30 days. The latter two are computed by taking the partial summation of the power spectrum computed from monthly connectivity time series. Figure 13c accounts for a fraction of Figure 13b due to interannual and seasonal variability (Fourier modes with the time period of 6 months or longer). Figure 13d accounts for a fraction of panel b due to eddy-induced (or intraseasonal) variability (Fourier modes with the time period less than 6 months).

$\Delta_G = 1$ km, maximum expected values of subgrid-scale diffusivity are $\gamma_t = 3.1 \times 10^4 \text{ cm}^2 \text{ s}^{-1}$ which is orders of magnitude smaller than the resolved scale eddy diffusivity and should have little influence on the connectivity patterns. For example, expected root mean square displacements due to subgrid-scale motions can be estimated as $(2\gamma_t T)^{1/2}$ [Taylor, 1921] and are smaller than 4.0 km, for a long (compared to correlation time) advection time of $T = 30$ days, and 0.8 km, for a short advection time of $T = 3$ days. Therefore horizontal subgrid-scale diffusivity will not be important in evaluating Lagrangian PDFs or coastal connectivity. Evaluating the importance of subgrid-scale vertical diffusivity (viscosity) will require substantial work (e.g., depending on particle-release depths, schemes to represent subgrid-scale motions, and more). This is an open question for a future work.

[42] The limited domain provides another issue for us to consider as water parcels that are advected to the domain boundary are lost from the system, although actually they may return. Hence some sites, especially those near the domain boundaries, may have reduced levels of connectivity due simply to this boundary effect. To illustrate this point, we computed particle residence (e-folding) times for released particles from each site (Figure 14). Values of residence time range from 5 to 50 days. The highest residence times are found for sites in the Santa Monica

Bay whereas sites near San Diego have the shortest residence times. High values of retention in the SCB are driven by the persistent SCB eddy which reduces the overall impacts of this boundary effect and the SCB will retain particles for a prolonged period of time. The low values off San Diego are caused partly by the mean southward transport there as these sites are located outside of the SCB eddy (Figure 14b; see also Dong *et al.* [2009]), and are partly due to the boundary effect. Similarly, sites near Point Conception, San Miguel and Santa Rosa (south shore) Islands have shorter residence time. The simplest, though numerically expensive, solution is to enlarge the domain. Another solution is to statistically estimate the number of particles that come back to the domain, and reseed them at the domain boundaries. This requires nontrivial investigations (future work).

[43] There are other processes (surface waves, etc) that are not included in the current ROMS simulations and may affect the predictions of coastal connectivity. For example, the dynamics of coastal boundary layers (e.g., influenced by surf-zone dynamics and flow-vegetation interactions) can alter particle dispersal patterns. As another example, Stokes drift might transport substantial numbers of particles toward the shore; this may have the potential to reduce the connection distances reported in this paper. While we have chosen a near surface (5 m) particle release and passive

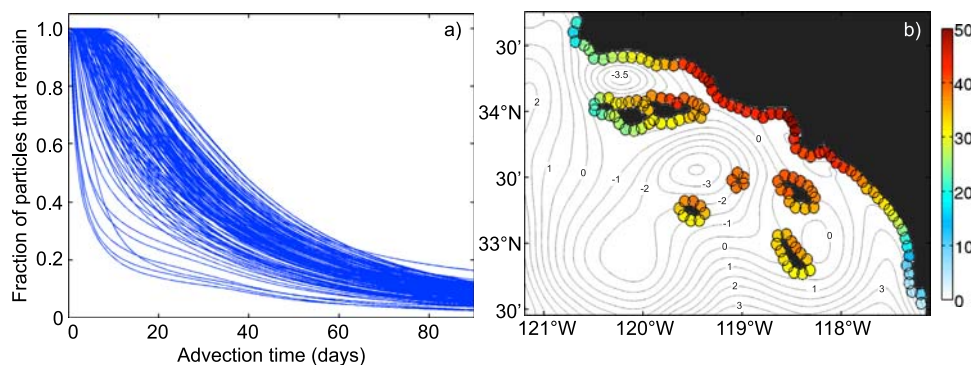


Figure 14. (a) Fraction of Lagrangian particles that remain in the domain for a given advection time in all Lagrangian particles released from each site. There are 135 lines, corresponding to 135 nearshore sites (see Figure 1). All Lagrangian particles released from 1996 to 2002 are used to compute the fraction regardless of the release season and year. (b) Residence (e-folding) time (days) computed from the residence probability on Figure 14a. The residence time is defined as the advection time for which the fraction of particles that stay within the domain decreases to $1/e$. The contours indicate the mean sea surface height in centimeters averaged over 1996–2002.

transport, the effect of the release depth and vertical positioning can be of importance for some situations.

[44] In summary, the ROMS model provides a good first assessment of connectivity patterns in the SCB. Eulerian statistics show good agreements with various observations [Dong *et al.*, 2009]. Lagrangian PDFs qualitatively agree with observations. Connectivity near the boundary may be underestimated, but the boundary effect is less substantial in the SCB due to the SCB eddy retention. The ROMS model has fine spatial resolution and captures the varying scales of motions that contain most of the kinetic energy that control dispersal patterns. Therefore we suggest that the model outputs are good enough to forecast the expected connectivity under a given climate condition. An obvious future direction is data assimilation. Data-driven models will give us further spatiotemporal resolutions in predictability and to operationalize these types of applications.

5.2. Applications of Lagrangian PDFs

[45] An important advantage of the Lagrangian PDF approach is that it can be used to predict future concentrations, at all locations in the domain, of important materials. For example, Lagrangian PDFs can be used to assess the risk from exposure of a pollutant emanating from a single source at location \mathbf{a} as

$$\langle c(\mathbf{x}, t_0 + T_e) \rangle = \int_{t_0}^{t_0 + T_r} \dot{c}(\mathbf{a}, t') f_X(\mathbf{x}; t_0 + T_e - t', \mathbf{a}) (\pi R^2) dt'. \quad (11)$$

where $\dot{c}(\mathbf{a}, t')$ is a pollutant input rate at time t' ; pollutant release starts at time t_0 and continues up to time $t_0 + T_r$; R is the radius of each site; $T_0 + T_e$ is an evaluation time; $\langle c(\mathbf{x}, t_0 + T_e) \rangle$ is the predicted (expected) pollutant concentrations at $t_0 + T_e$, and $T_e \geq T_r$. A sample pollutant spread from Santa Monica Bay is shown in Figure 15 for $T_r = 10, 30$ days and $T_e = 30, 60$ days. Nearshore exposure to the pollutant increases as T_r increases, and decreases as T_e increases. The pollutant is mostly transported poleward for all cases, but the concentration distribution differs for a different choice

of T_r and T_e . For instance, the pollutant mostly remains within Santa Monica Bay for a short-release case ($T_r = 10, T_e = 30$ days; Figure 15a), whereas for a long-release case ($T_r = 30, T_e = 60$ days), the concentration within the SB Channel becomes substantially higher, and mainland sites between Ventura and Point Conception are exposed to a similar level of pollution. Thus the risk assessment depends on the quantification of expected connectivity from the source site to all other sites in the region as a function of timescale from pollutant release and of evaluation time.

[46] For many nearshore fish species, larval fish are transported to remote locations by ocean currents. There, they can recruit to the adult population. For fisheries management, recruitment of new individuals to a fishery sets an upper bound for what can be caught sustainably [e.g., Hilborn and Walters, 2001]. Within our framework, we can use estimates of coastal connectivity to estimate the number of new recruits. Given the larval production at all source sites (P_j , where $j = 1, 2, \dots, N_j$) and the connectivity from site j to site i , $C_{ji}(\tau)$, corresponding to planktonic larval durations (τ) and spawning season, the number of new recruits at a given site i (R_i) can be expressed as

$$R_i = \beta_i \sum_{j=1}^{N_j} (1 - m) P_j C_{ji}(\tau) \quad (12)$$

where m is larval mortality, and β_i is the fraction of larvae that successfully recruit to adults in all arriving larvae. Different species have different spawning seasons and different planktonic larval duration. Accordingly, as described above, connectivity patterns can be greatly different for different species (see Figures 7–11). Therefore knowing species-specific connectivity is essential in predicting future fish recruitment and stock [e.g., Cowen *et al.*, 2000; Hilborn and Walters, 2001; Cowen *et al.*, 2006].

[47] Marine protected areas (MPAs) or no-take zones are areas of the ocean restricted to fishing for the processes of fisheries management. Important to the efficacy of a marine protected area is the notion of larval spillover or the contribution of new fish to other places from the protected

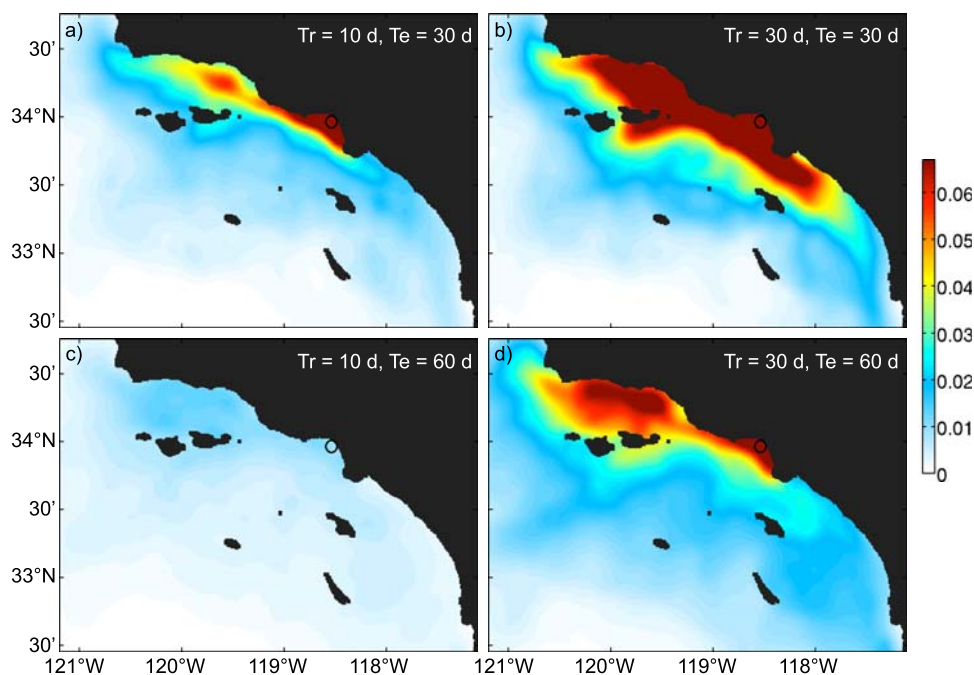


Figure 15. Sample prediction of pollutant spread from Santa Monica Bay (site 32) in winter season as a function of release duration (T_r) and evaluation time (T_e). The pollutant release starts at time t_0 and continues until $t_0 + T_r$. The pollutant distribution is assessed at time $t_0 + T_e$. Four different cases are shown here: (a) $T_r = 10$, $T_e = 30$ days; (b) $T_r = 30$, $T_e = 30$ days; (c) $T_r = 10$, $T_e = 60$ days; and (d) $T_r = 30$, $T_e = 60$ days. The predictions are determined by equation (11), given $\dot{c}(\mathbf{a}, t) = 1 \text{ mol m}^{-3} \text{ d}^{-1}$ of pollutant input rate. The colors indicate the pollutant concentration in mol m^{-3} .

area [e.g., *Botsford et al.*, 2003]. The Lagrangian PDF approach can be used to describe larval spillover for a range of sedentary or sessile marine species in the SCB. The planktonic larval duration (PLD) is a species specific trait and by finding the mean connection times between sites in the SCB we can gain insight as to which locations, as an MPA, would potentially spillover what species and to where.

[48] We define the mean connection time between site j and site i as the mean advection time weighted by $C_{ji}(\tau)$, i.e.,

$$T_{ji} = \int_0^\infty C_{ji}(\tau)\tau d\tau / \int_0^\infty C_{ji}(\tau)d\tau \quad (13)$$

We estimate the mean connection time by setting the upper limit of the integral in equation (13) to 120 days. Sample mean connection times from four different sites (including ongoing MPA sites) are shown in Figure 16. Connection times among the SB Channel sites are relatively short (10–20 days), whereas connection from inner SB Channel to outer SB Channel is much longer (40–60 days) (Figures 16a and 16b), reflecting local retention in the SCB (see Figure 4). Mean connection time from Oceanside increases along the path of the counterclockwise SCB eddy, i.e., about 20 days to Palos Verdes Peninsula, 40 days to the SB Channel and Point Conception, and 2 months to the outer limb of the SCB eddy (Figure 16c). Mean connection times from Santa Catalina Island show less spatial variations, less

than 50 days to any sites (Figure 16d).

[49] Planktonic larval durations (PLDs) of marine species range from a few days to several months [e.g., *Siegel et al.*, 2003]. Spillover of species with relatively short PLDs (within a few weeks; e.g., red abalone) will be, on average, limited to local areas, while species with longer PLDs (several months; e.g., sea urchin, rockfish and lingcod) can spill over to all sites in the SCB (Figure 16), although at the same time many of them will be lost to outside of the domain (Figure 14d). Species with moderate PLDs (a month; e.g., kelp bass) will be in between. The mean connection time is not proportional to the Euclidean distance between sites. These considerations need to be made in designing MPAs. For example, species with short PLDs will spillover from Oceanside to Long Beach, but not to Southern Islands, despite that they are nearly equidistant (Figure 16d).

[50] Effective marine management depends upon an explicit knowledge of dispersal as a result of ocean circulation. We have presented three applications, the dispersal of marine pollutants and the dispersal of marine species larvae and its implications to fisheries management, in particular marine protected areas. Indeed, an understanding of the spatial distribution of any resource or contaminant of interest (that is subject to the ocean currents) will benefit from the Lagrangian PDF analysis presented here.

6. Summary and Conclusions

[51] Assessment of water parcel connectivity in the SCB has been made by using high-resolution ROMS simulations

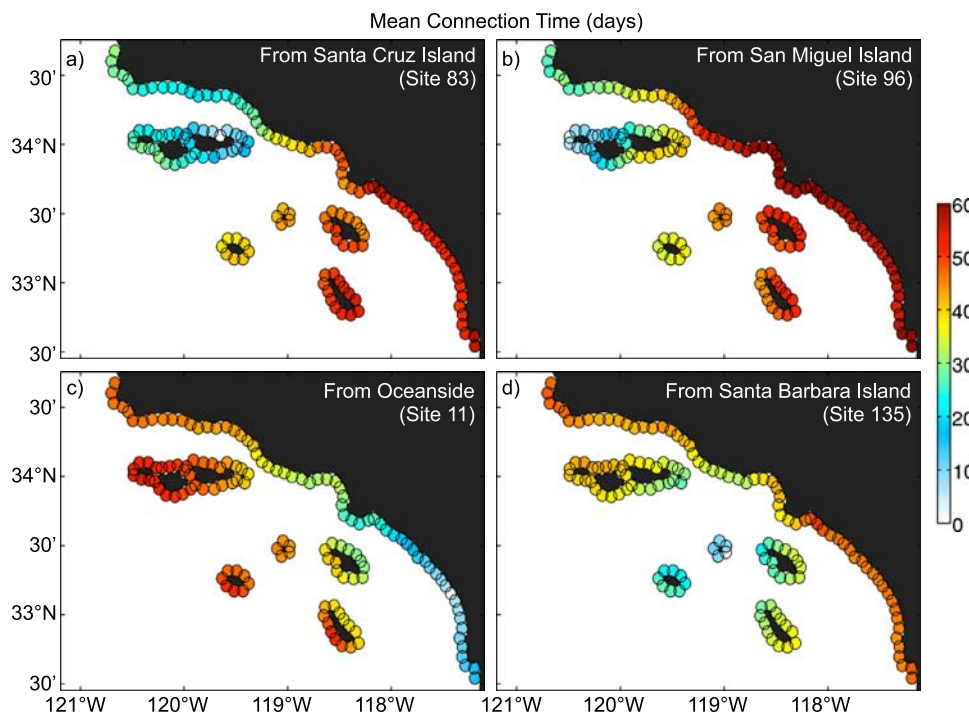


Figure 16. Mean connection times from the sites on the shore of (a) Chinese Harbor (site 83), (b) San Miguel Island (site 96), (c) Oceanside (site 11), and (d) Santa Barbara Island (site 135) to all nearshore sites. The release sites are indicated with white circles. The mean connectivity times are determined by the connectivity-weighted averages of the advection time, as described by equation (13), given connectivity matrices for the advection time of $\tau = 1, 2, \dots, 120$ days. Colors indicate the mean connection time in days. All Lagrangian particles released from all sites from 1996 to 2002 are used to compute the mean connection times.

validated against available observations. The simulated dispersal patterns are consistent with oceanographic patterns documented in the literature. Expected dispersal patterns (and coastal connectivity) show strong dependencies on particle-release location, season and year, reflecting annual and interannual circulation patterns in the SCB. Lagrangian PDFs from mainland release sites clearly reflect the Southern California Countercurrent. Regional retention of water parcels coincide with locations showing cyclonic circulations. Realizations vary month to month, reflecting intrinsic variability induced by eddy motions. The intrinsic intra-seasonal variability is as much as the mean and seasonal/interannual variability, and thus sets a strong source of uncertainty in connectivity patterns. Connectivity patterns change as a function of advection time, and in general, substantial water mass is transported from mainland sites to Islands sites, but not the other way around. Hence the connection among sites cannot be represented with Euclidean distance between sites. The future points to these techniques holding in a variety of applications. One issue is intrinsic eddy-driven variability which may be solved by data assimilation models for real-time forecasts. We will need not only Eulerian validations, but also Lagrangian validations of circulation models by taking advantages of existing and ongoing observations [e.g., drifters, population genetics, microchemistry and fish (invertebrate) recruitment data]. The procedures presented here can be

applied to other sites, given appropriate high-resolution model outputs.

Appendix A: PDF Methods Including Diffusion and Reactions

[52] The Lagrangian PDF method used in this study does not account for mixing and chemical (biological) reactions of materials. The future value of materials can be predicted by knowing the initial material concentrations and Lagrangian PDFs as in equation (6) only if the composition of materials are unchanged during the water-parcel transport. The assumption may not be relevant for some applications because materials associated with a water parcel may be diluted by mixing processes, and may be altered due to the chemical (biological) reaction of materials. In the last decades, PDF methods have been extended to account for these effects [e.g., *Pope, 1994*]. Here we summarize this modeling approach, which may be useful for ecological and other applications.

[53] This PDF modeling approach describes the chemical (biological) composition of a water parcel at a given location and time. Consider a composite of M materials ($\phi_1, \phi_2, \dots, \phi_M$) that are introduced at a source (\mathbf{a}). Each realization leads to different material distributions [$\phi_\alpha(\mathbf{x}, t)$, $\alpha = 1, 2, \dots, M$] due to intrinsic eddy-variability (Figure 2) and mixing and reactions. The PDF method describes the probability densities of material composition at location \mathbf{x}

and time t , denoted here as $f_\phi(\psi; \mathbf{x}, t)$, where $\psi = (\psi_1, \psi_2, \dots, \psi_M)$ is the sample space variable for material concentrations. This approach is essentially an extension of equation (6) to multiple reactive materials.

[54] There exists a technique to derive a governing equation for the composition PDF from a fundamental advection-diffusion-reaction equation [e.g., *Pope*, 1985]. The evolution of material composition can be expressed, for instance, as

$$\frac{\partial \phi_\alpha}{\partial t} + \frac{\partial u_i \phi_\alpha}{\partial x_i} = \frac{\partial}{\partial x_i} \left(\kappa \frac{\partial \phi_\alpha}{\partial x_i} \right) + \omega_\alpha(\phi) \quad (\text{A1})$$

where $\alpha = 1, 2, \dots, M$ identifies each material (species), $u_i(\mathbf{x}, t)$ is the Eulerian velocity, κ is the diffusion coefficient, and $\omega_\alpha(\phi)$ is the reaction term for material α , which is a function of all materials. In this case, the composition PDF or $f_\phi(\psi; \mathbf{x}, t)$ obeys

$$\frac{\partial f_\phi}{\partial t} + \frac{\partial \langle u_i | \psi \rangle f_\phi}{\partial x_i} = \frac{\partial \langle \kappa \nabla^2 \phi_\alpha | \psi \rangle f_\phi}{\partial \psi_\alpha} - \frac{\partial \omega_\alpha f_\phi}{\partial \psi_\alpha} \quad (\text{A2})$$

where $\langle u_i | \psi \rangle$ and $\langle \kappa \nabla^2 \phi_\alpha | \psi \rangle$ are, respectively, the ensemble-average of $u_i(\mathbf{x}, t)$ and $\kappa \nabla^2 \phi_\alpha(\mathbf{x}, t)$ conditional upon a set of composition values $\phi(\mathbf{x}, t) = \psi$.

[55] The composition PDF equation is not closed, and requires modeling of the two conditional means, in terms of velocity and diffusion. A variety of physically sound models have been developed for the unclosed terms [e.g., *Pope*, 1985; *Chen et al.*, 1989; *Colucci et al.*, 1998; *Mitarai et al.*, 2003]. For example, following *Colucci et al.* [1998],

$$\frac{\partial f_\phi}{\partial t} + \frac{\partial \langle u_i | \psi \rangle f_\phi}{\partial x_i} = \frac{\partial}{\partial x_i} \left((\kappa + \kappa_t) \frac{\partial f_\phi}{\partial x_i} \right) + \frac{\partial \Omega (\psi_\alpha - \langle \phi_\alpha \rangle) f_\phi}{\partial \psi_\alpha} - \frac{\partial \omega_\alpha f_\phi}{\partial \psi_\alpha}, \quad (\text{A3})$$

where Ω is a mixing frequency constant [*Pope*, 2000] and κ_t is eddy diffusivity, and the bracket $\langle \cdot \rangle$ is an ensemble-averaging operator. By taking the first moment of this equation, we obtain the mean composition equation, i.e.,

$$\frac{\partial \langle \phi_\alpha \rangle}{\partial t} + \frac{\partial \langle u_i | \phi_\alpha \rangle}{\partial x_i} = \frac{\partial}{\partial x_i} \left((\kappa + \kappa_t) \frac{\partial \langle \phi_\alpha \rangle}{\partial x_i} \right) + \langle \omega_\alpha(\phi) \rangle. \quad (\text{A4})$$

The same exact equation can be obtained from equation (A1) by using a conventional modeling approach, i.e., taking an ensemble average of both sides of the equation and assuming $\langle u_i | \phi_\alpha \rangle = \kappa_t \nabla \phi_\alpha(\mathbf{x}, t)$ [e.g., *LaCasce*, 2008]. Note that equation (A4) requires the modeling of the mean reaction term, whereas equation (A3) does not.

[56] The closed composition-PDF equation, equation (A3), can be integrated directly, but it usually requires much computational resources. Alternatively, the composite-PDF evolution equation can be indirectly integrated through Monte Carlo simulations of an equivalent stochastic particle

system, which can be obtained through the Fokker-Planck formalism [e.g., *Gardiner*, 1997] as

$$dX_i^* = \left[\langle u_i \rangle + \frac{\partial (\kappa + \kappa_t)}{\partial x_i} \right] dt + [2(\kappa + \kappa_t)]^{1/2} dW_i, \quad (\text{A5})$$

$$\frac{d\phi_\alpha^*}{dt} = \Omega(\phi_\alpha^* - \langle \phi_\alpha \rangle) + \omega_\alpha(\phi^*). \quad (\text{A6})$$

where X^* and ϕ_α^* , respectively, indicate the position and composition of a stochastic particle; and W_i is the Wiener process [e.g., *Gardiner*, 1997]. The composition PDF, $f_\phi(\psi; \mathbf{x}, t)$, can be obtained by making a histogram of the composition of the particles within a specified area centered at \mathbf{x} (e.g., a numerical grid cell) or as in equation (5). Similarly, the mean composition, $\langle \phi_\alpha(\mathbf{x}, t) \rangle$, can be given as the mean particle composition.

[57] Theoretically, Lagrangian PDFs shown in study (Figures 3–6) can be reproduced using the stochastic particle equation (equation (A5)), given the mean velocity fields and eddy diffusivity deduced from the ROMS model or by other means (e.g., climatology estimated from observations). Lagrangian PDFs can be determined by counting the number of stochastic particles found within a defined area similarly to equation (4). This modeling approach is numerically much less expensive than Lagrangian particle tracking methods, because it does not require a series of flow fields, but only statistics. The effects of mixing and reactions, if necessarily, can be assessed by integrating equation (A6) at the same time. In this study, we did not employ equation (A5) since the prediction depends on the modeling accuracy of the unclosed terms and estimates of eddy diffusivity. The model predictability has been tested in engineering applications, e.g., against direct numerical simulations of Navier-Stokes equations of chemically reacting turbulent flows [e.g., *Colucci et al.*, 1998; *Mitarai et al.*, 2003] and piloted turbulent diffusion flame experiments [e.g., *Lindstedt et al.*, 2000], but not yet for oceanographic flows.

[58] **Acknowledgments.** The authors acknowledge a series of enlightening discussions with Steven Gaines, Bob Warner, Chris Costello, Bruce Kendall, Libe Washburn, Carter Ohlmann, Jenn Caselle, Brian Kinlan, Tim Chaffey, and Crow White. We thank Eileen Idica for aiding in many aspects of this work. This work was supported by the National Science Foundation (NSF grant 0308440, OCE 06-23011), California Coastal Conservancy (04078.05LA), University of California Coastal Environmental Quality Initiative, National Oceanic and Atmospheric Administration (NA17RJ1231), National Aeronautics and Space Administration (NNX08AI84G), and USGS/EPA project.

References

- Beckenbach, E., and L. Washburn (2004), Low-frequency waves in the Santa Barbara Channel observed by high-frequency radar, *J. Geophys. Res.*, *109*, C02010, doi:10.1029/2003JC001999.
- Bernstein, R., L. Breaker, and R. Whritner (1977), California Current eddy formation: Ship, air, and satellite results, *Science*, *195*(4276), 353–359.
- Black, T. (1994), The new NMC mesoscale eta-model: Description and forecast examples, *Weather Forecast.*, *9*(2), 265–278.
- Bograd, S., and R. Lynn (2003), Long-term variability in the Southern California Current System, *Deep Sea Res., Part II*, *50*(14–16), 2355–2370, doi:10.1016/S0967-0645(03)00131-0.

- Bograd, S., et al. (2000), The state of the California Current, 1999–2000: Forward to a new regime?, *Calif. Coop. Ocean. Fish. Invest. Rep.*, *41*, 26–52.
- Botsford, L., F. Micheli, and A. Hastings (2003), Principles for the design of marine reserves, *Ecol. Appl.*, *13*(1), S25–S31.
- Bray, N. A., A. Keyes, and W. M. L. Morawitz (1999), The California Current system in the Southern California Bight and the Santa Barbara Channel, *J. Geophys. Res.*, *104*(C4), 7695–7714.
- Brink, K., and R. Muench (1986), Circulation in the Point Conception Santa-Barbara Channel region, *J. Geophys. Res.*, *91*(C1), 877–895.
- Carr, S. D., X. J. Capet, J. C. McWilliams, J. T. Pennington, and F. P. Chavez (2008), The influence of diel vertical migration on zooplankton transport and recruitment in an upwelling region: Estimates from a coupled behavioral-physical model, *Fish. Oceanogr.*, *17*(1), 1–15, doi:10.1111/j.1365-2419.2007.00447.x.
- Carton, J., G. Chepurin, and X. Cao (2000a), A simple ocean data assimilation analysis of the global upper ocean 1950–95: Part II. Results, *J. Phys. Oceanogr.*, *30*(2), 311–326.
- Carton, J., G. Chepurin, X. Cao, and B. Giese (2000b), A simple ocean data assimilation analysis of the global upper ocean 1950–95: Part I. Methodology, *J. Phys. Oceanogr.*, *30*(2), 294–309.
- Chen, H., S. Chen, and R. Kraichnan (1989), Probability-distribution of a stochastically advected scalar field, *Phys. Rev. Lett.*, *63*(24), 2657–2660.
- Colucci, P., F. Jaberi, P. Givi, and S. Pope (1998), Filtered density function for large eddy simulation of turbulent reacting flows, *Phys. Fluids*, *10*(2), 499–515.
- Conil, S., and A. Hall (2006), Local regimes of atmospheric variability: A case study of southern California, *J. Clim.*, *19*(17), 4308–4325.
- Corsin, S. (1962), Theories of turbulent dispersion, in *Mécanique de la Turbulence*, pp. 27–52, CNRS, Paris.
- Cowen, R., K. Lwiza, S. Sponaugle, C. Paris, and D. Olson (2000), Connectivity of marine populations: Open or closed?, *Science*, *287*(5454), 857–859.
- Cowen, R., C. Paris, and A. Srinivasan (2006), Scaling of connectivity in marine populations, *Science*, *311*(5760), 522–527, doi:10.1126/science.1122039.
- Davis, R. (1987), Modeling eddy transport of passive tracers, *J. Mar. Res.*, *45*(3), 635–666.
- Dever, E., and C. Winant (2002), The evolution and depth structure of shelf and slope temperatures and velocities during the 1997–1998 El Niño near Point Conception, California, *Prog. Oceanogr.*, *54*(1–4), 77–103, doi:10.1016/S0079-6611(02)00044-7.
- Dever, E., M. Hendershott, and C. Winant (1998), Statistical aspects of surface drifter observations of circulation in the Santa Barbara Channel, *J. Geophys. Res.*, *103*(C11), 24,781–24,797.
- Di Lorenzo, E. (2003), Seasonal dynamics of the surface circulation in the Southern California Current System, *Deep Sea Res., Part II*, *50*(14–16), 2371–2388, doi:10.1016/S0967-0645(03)00125-5.
- Dong, C., and J. C. McWilliams (2007), A numerical study of island wakes in the Southern California Bight, *Cont. Shelf Res.*, *27*(9), 1233–1248, doi:10.1016/j.csr.2007.01.016.
- Dong, C., E. Idica, and J. McWilliams (2009), Circulation and multi-scale variability in the Southern California Bight, *Prog. Oceanogr.*, doi:10.1016/j.pocean.2009.07.005, in press.
- Durrant, D. R. (1999), *Numerical Methods for Wave Equations in Geophysical Fluid Dynamics*, Springer, New York.
- Fischer, H. B., J. E. List, R. C. Koh, J. Imberger, and N. H. Brooks (1979), *Mixing in Inland and Coastal Waters*, Academic Press, New York.
- Gaines, S., B. Gaylord, and J. Largier (2003), Avoiding current oversights in marine reserve design, *Ecol. Appl.*, *13*(1), S32–S46.
- Gardiner, C. W. (1997), *Handbook of Stochastic Methods for Physics, Chemistry and the Natural Sciences*, Springer, Berlin, Germany.
- Grant, S., J. Kim, B. Jones, S. Jenkins, J. Wasyl, and C. Cudaback (2005), Surf zone entrainment, along-shore transport, and human health implications of pollution from tidal outlets, *J. Geophys. Res.*, *110*, C10025, doi:10.1029/2004JC002401.
- Harms, S., and C. Winant (1998), Characteristic patterns of the circulation in the Santa Barbara Channel, *J. Geophys. Res.*, *103*(C2), 3041–3065.
- Hickey, B. (1979), The California Current system: Hypotheses and facts, *Prog. Oceanogr.*, *8*, 191–279.
- Hickey, B. (1992), Circulation over the Santa-Monica San-Pedro Basin and Shelf, *Prog. Oceanogr.*, *30*(1–4), 37–115.
- Hickey, B. (1993), Physical oceanography, in *Ecology of the Southern California Bight: A Synthesis and Interpretation*, edited by M. D. Dailey, D. J. Reish, and J. W. Anderson, pp. 19–70, Univ. of Calif. Press, Berkeley, Calif.
- Hickey, B., E. Dobbins, and S. Allen (2003), Local and remote forcing of currents and temperature in the central Southern California Bight, *J. Geophys. Res.*, *108*(C3), 3081, doi:10.1029/2000JC000313.
- Hilborn, R., and C. J. Walters (2001), *Quantitative Fisheries Stock Assessment: Choice, Dynamics and Uncertainty*, Kluwer, Boston, Mass.
- Hughes, M., A. Hall, and R. G. Fovell (2007), Dynamical controls on the diurnal cycle of temperature in complex topography, *Clim. Dyn.*, *29*(2–3), 277–292, doi:10.1007/s00382-007-0239-8.
- Jackson, G., and R. Strathmann (1981), Larval mortality from offshore mixing as a link between pre-competent and competent periods of development, *Am. Nat.*, *118*(1), 16–26.
- Kinlan, B., and S. Gaines (2003), Propagule dispersal in marine and terrestrial environments: A community perspective, *Ecology*, *84*(8), 2007–2020.
- LaCasce, J. H. (2008), Statistics from Lagrangian observations, *Prog. Oceanogr.*, *77*(1), 1–29, doi:10.1016/j.pocean.2008.02.002.
- Largier, J. (2003), Considerations in estimating larval dispersal distances from oceanographic data, *Ecol. Appl.*, *13*(1), S71–S89.
- Lindstedt, R., S. Louloudi, and E. Vaos (2000), Joint scalar probability density function modeling of pollutant formation in piloted turbulent jet diffusion flames with comprehensive chemistry, *Proc. Combust. Inst.*, *28*, 149–156.
- Lynn, R., and S. Bograd (2002), Dynamic evolution of the 1997–1999 El Niño-La Niña cycle in the southern California Current System, *Prog. Oceanogr.*, *54*(1–4), 59–75, doi:10.1016/S0079-6611(02)00043-5.
- Lynn, R., and J. Simpson (1987), The California Current System: The seasonal variability of its physical characteristics, *J. Geophys. Res.*, *92*(C12), 12,947–12,966.
- Mitarai, S., J. Riley, and G. Kosály (2003), A Lagrangian study of scalar diffusion in isotropic turbulence with chemical reaction, *Phys. Fluids*, *15*(12), 3856–3866, doi:10.1063/1.1622950.
- Nishimoto, M., and L. Washburn (2002), Patterns of coastal eddy circulation and abundance of pelagic juvenile fish in the Santa Barbara Channel, California, USA, *Mar. Ecol. Prog. Ser.*, *241*, 183–199.
- Oey, L., C. Winant, E. Dever, W. Johnson, and D. Wang (2004), A model of the near-surface circulation of the Santa Barbara Channel: Comparison with observations and dynamical interpretations, *J. Phys. Oceanogr.*, *34*(1), 23–43.
- Otero, M., and D. Siegel (2004), Spatial and temporal characteristics of sediment plumes and phytoplankton blooms in the Santa Barbara Channel, *Deep Sea Res., Part II*, *51*(10–11), 1129–1149, doi:10.1016/j.dsr2.2004.04.004.
- Penven, P., L. Debreu, P. Marchesiello, and J. McWilliams (2006), Evaluation and application of the ROMS 1-way embedding procedure to the central California upwelling system, *Ocean Modell.*, *12*(1–2), 157–187, doi:10.1016/j.ocemod.2005.05.002.
- Pfeiffer-Herbert, A. S., M. A. McManus, P. T. Raimondi, Y. Chao, and F. Chai (2007), Dispersal of barnacle larvae along the central California coast: A modeling study, *Limnol. Oceanogr.*, *52*(4), 1559–1569.
- Pope, S. (1985), PDF methods for turbulent reactive flows, *Prog. Energy Combust. Sci.*, *11*(2), 119–192.
- Pope, S. (1994), Lagrangian PDF methods for turbulent flows, *Annu. Rev. Fluid Mech.*, *26*, 23–63.
- Pope, S. B. (2000), *Turbulent Flows*, Cambridge Univ. Press, New York.
- Poulain, P., and P. Niiler (1989), Statistical-analysis of the surface circulation in the California Current System using satellite-tracked drifters, *J. Phys. Oceanogr.*, *19*(10), 1588–1603.
- Roughgarden, J., S. Gaines, and H. Possingham (1988), Recruitment dynamics in complex life-cycles, *Science*, *241*(4872), 1460–1466.
- Shchepetkin, A., and J. McWilliams (2005), The regional oceanic modeling system (ROMS): A split-explicit, free-surface, topography-following-coordinate oceanic model, *Ocean Modell.*, *9*(4), 347–404, doi:10.1016/j.ocemod.2004.08.002.
- Shchepetkin, A., and J. O'Brien (1996), A physically consistent formulation of lateral friction in shallow-water equation ocean models, *Mon. Weather Rev.*, *124*(6), 1285–1300.
- Schwing, F., C. Moore, S. Ralston, and K. Sakuma (2000), Record coastal upwelling in the California Current in 1999, *Calif. Coop. Ocean. Fish. Invest. Rep.*, *41*, 148–160.
- Siegel, D., B. Kinlan, B. Gaylord, and S. Gaines (2003), Lagrangian descriptions of marine larval dispersion, *Mar. Ecol. Prog. Ser.*, *260*, 83–96.
- Siegel, D. A., S. Mitarai, C. J. Costello, S. D. Gaines, B. E. Kendall, R. R. Warner, and K. B. Winters (2008), The stochastic nature of larval connectivity among nearshore marine populations, *Proc. Natl. Acad. Sci. U. S. A.*, *105*(26), 8974–8979, doi:10.1073/pnas.0802544105.
- Smagorinsky, J. (1993), Some historical remarks on the use of nonlinear viscosities, in *Large Eddy Simulation of Complex Engineering and Geophysical Flows*, edited by B. Galperin and S. A. Orszag, pp. 3–36, Cambridge Univ. Press, Cambridge, U. K.

- Sverdrup, H., and R. Fleming (1941), The waters off the coast of Southern California, *Scripps Ins. Oceanogr. Bull.*, 4, 261–387.
- Swenson, M., and P. Niiler (1996), Statistical analysis of the surface circulation of the California Current, *J. Geophys. Res.*, 101(C10), 22,631–22,645.
- Taylor, G. (1921), Diffusion by continuous movements, *Proc. Lond. Math. Soc.*, 20, 196–202.
- Tennekes, H., and J. L. Lumley (1972), *A First Course in Turbulence*, MIT Press, Cambridge, Mass.
- Winant, C., and C. Dorman (1997), Seasonal patterns of surface wind stress and heat flux over the Southern California Bight, *J. Geophys. Res.*, 102(C3), 5641–5653.
- Winant, C., D. Alden, E. Dever, K. Edwards, and M. Hendershott (1999), Near-surface trajectories off central and southern California, *J. Geophys. Res.*, 104(C7), 15,713–15,726.
-
- C. Dong and J. C. McWilliams, Institute of Geophysics and Planetary Physics, University of California, 405 Hilgard Avenue, Los Angeles, CA 90095, USA. (cdong@atmos.ucla.edu; jcm@atmos.ucla.edu)
- S. Mitarai, D. A. Siegel, and J. R. Watson, Institute for Computational Earth System Science, University of California, 6844 Ellison Hall, Santa Barbara, CA 93106, USA. (satoshi@icess.ucsb.edu; davey@icess.ucsb.edu; watson@icess.ucsb.edu)